

# Wetting Effect on Patterned Substrates

Fei Wang,\* Yanchen Wu, and Britta Nestler

A droplet deposited on a solid substrate leads to the wetting phenomenon. A natural observation is the lotus effect, known for its superhydrophobicity. This special feature is engendered by the structured microstructure of the lotus leaf, namely, surface heterogeneity, as explained by the quintessential Cassie–Wenzel theory (CWT). In this work, recent designs of functional substrates are overviewed based on the CWT via manipulating the contact area between the liquid and the solid substrate as well as the intrinsic Young's contact angle. Moreover, the limitation of the CWT is discussed. When the droplet size is comparable to the surface heterogeneity, anisotropic wetting morphology often appears, which is beyond the scope of the Cassie–Wenzel work. In this case, several recent studies addressing the anisotropic wetting effect on chemically and mechanically patterned substrates are elucidated. Surface designs for anisotropic wetting morphologies are summarized with respect to the shape and the arrangement of the surface heterogeneity, the droplet volume, the deposition position of the droplet, as well as the mean curvature of the surface heterogeneity. A thermodynamic interpretation for the wetting effect and the corresponding open questions are presented at the end.

beasts.<sup>[20,21]</sup> Sometimes, the water is repelled by the surface, such as the kingfisher's feather to keep dry;<sup>[22]</sup> sometimes, the water is preferred by the surface, for example, the harvest of water via the back of *Stenocara*<sup>[23]</sup> and Namib desert beetles<sup>[24]</sup> (see refs. [25, 26] for beetle-inspired surfaces). In our daily lives, we see the wetting phenomena on the top of umbrella while raining,<sup>[27,28]</sup> on the surface of glass while fogging,<sup>[29,30]</sup> and on the surface of wall while icing.<sup>[31]</sup> For practical applications, the wetting effect with the solid–liquid interaction plays a non-negligible role and is often involved in materials design. Typical examples for the desired materials are self-cleaning,<sup>[32–35]</sup> anti-fouling,<sup>[36–38]</sup> anti-fogging<sup>[39,40]</sup> of solid substrates including glasses, metals, and ceramics. These functionalities may be achieved by changing the surface chemistry,<sup>[41]</sup> for example coating,<sup>[42,43]</sup> or by modifying the surface microstructures,<sup>[44–47]</sup> which are known to be chemically and mechanically patterned substrates, respectively. On these patterned

substrates, we sometimes want the liquid to detach from the solid substrate with a relatively small roll-off angle and sometimes require a strong adhesion of the solid wall to the liquid. The interaction between the liquid and the solid substrate is characterized by the wettability.

The wettability of a droplet on a solid substrate is usually quantified by the apparent contact angle  $\theta^*$  (Figure 2a,b), which is measured at the triple junction where the solid, liquid, and surrounding phases meet. On the homogeneous and heterogeneous substrates, the apparent contact angle follows Young's law<sup>[51]</sup> and Cassie–Wenzel theory,<sup>[52,53]</sup> respectively. When  $\theta^*$  is greater than  $90^\circ$ , the system is said to be hydrophobic; otherwise, we call it hydrophilicity; an apparent contact angle of  $90^\circ$  is termed as the neutral state. As shown in Figure 3a,b, a water droplet on the leaf of a lotus<sup>[54]</sup> and the petal of a rose<sup>[55]</sup> has an apparent contact angle greater than  $90^\circ$ , exhibiting a superhydrophobic property. Another two natural observations for the wetting effect of superhydrophobicity is the skin of filefish (Figure 3c) and the wings of a butterfly (Figure 3d). The apparent contact angle of oil in the environment of water on the skin of filefish is around  $156.1^\circ$ . This observation has inspired the fabrication of artificial fish skin, which may be used for underwater oleophobic materials. The apparent contact angle of water on the natural wing of the butterfly is about  $151.5^\circ$ , which shows superhydrophobicity as well. Inspired by this marvelous property, scientists have fabricated butterfly-inspired functional materials for different applications, such as intelligent surfaces,<sup>[56,57]</sup> optical devices,<sup>[58,59]</sup>

## 1. Introduction

Depositing a certain volume of liquid on a solid substrate leads to the wetting effect<sup>[1,2]</sup> (for soft and deformable substrates, see ref. [3]). This phenomenon is observed omnipresent in nature<sup>[4–6]</sup> and for materials design<sup>[4,7,8]</sup> (see Figure 1). For example, a series of dew is often dispersed on the petals of flowers,<sup>[9]</sup> and on the leaves of plants, such as *Salvinia molesta*,<sup>[10,11]</sup> the lotus,<sup>[12,13]</sup> and *Oryza sativa*.<sup>[14,15]</sup> The dispersion of water droplet is also observed on the feather of birds,<sup>[16,17]</sup> the wing of bugs,<sup>[18,19]</sup> and the skin of

F. Wang, Y. Wu, B. Nestler  
Institute for Applied Materials - Microstructure Modelling and Simulation (IAM-MMS)  
Karlsruhe Institute of Technology (KIT)  
Strasse am Forum 7, 76131 Karlsruhe, Germany  
E-mail: fei.wang@kit.edu

B. Nestler  
Institute of Digital Materials Science  
Karlsruhe University of Applied Sciences  
Moltkestrasse 30, 76133 Karlsruhe, Germany

 The ORCID identification number(s) for the author(s) of this article can be found under <https://doi.org/10.1002/adma.202210745>

© 2023 The Authors. Advanced Materials published by Wiley-VCH GmbH. This is an open access article under the terms of the Creative Commons Attribution License, which permits use, distribution and reproduction in any medium, provided the original work is properly cited.

DOI: 10.1002/adma.202210745

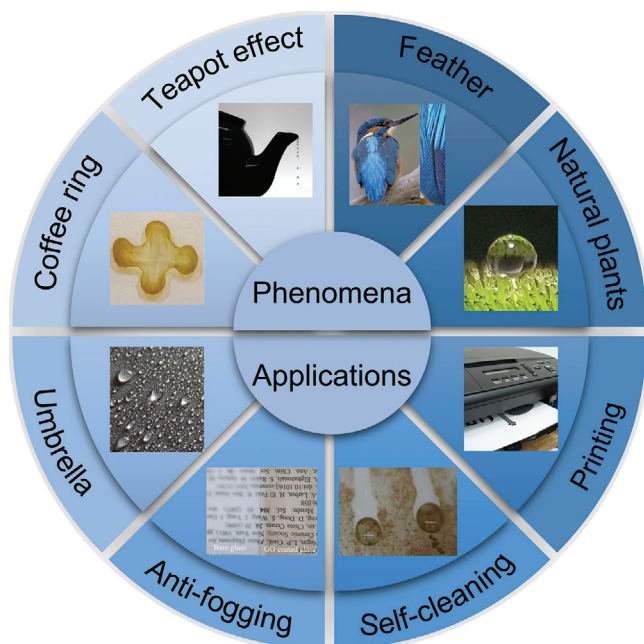


**Figure 1.** Phenomena and applications of wetting effect. Natural Plants: Water droplet on the leaf of *Salvinia molesta*. Reproduced under the terms of the CC-BY Creative Commons Attribution 4.0 International license (<https://creativecommons.org/licenses/by/4.0/>).<sup>[10]</sup> Copyright 2022, The Authors, published by Springer Nature. Feather: Kingfisher feathers to keep dry. Reproduced with permission.<sup>[22]</sup> Copyright 2011, Company of Biologists. Teapot effect: The water is confined at the edge of the teapot, reuse with permissions,<sup>[48]</sup> Copyright 2010, American Physical Society. Coffee-ring: Coffee-stain on a glass surface after drying of a coffee droplet. Reproduced with permission.<sup>[49]</sup> Copyright 2015, Elsevier. Umbrella: Water droplets on umbrella. Reproduced with permissions.<sup>[28]</sup> Copyright 2014, ICE Publishing. Printing: Inkjet printing on patterned substrate. Reproduced with permission.<sup>[50]</sup> Copyright 2013, Association for Computing Machinery. Application of self cleaning: Self cleaning surface. Reproduced with permission.<sup>[31]</sup> Copyright 2017, IJEREE. Application of anti-fogging: Anti-fogging glass. Reproduced with permission.<sup>[29]</sup> Copyright 2016, Elsevier.

biological sensors,<sup>[60]</sup> cell culture,<sup>[61]</sup> self-cleaning surfaces,<sup>[32]</sup> to cite a few. A comprehensive review of butterfly-inspired functional materials has been provided in ref. [62]. When the wing of the butterfly is covered by poly(ethylene glycol) diacrylate (gray area on the right wing in Figure 3d), the surface becomes hydrophilic. Apart from the natural observations, man-made functional materials have been synthesized based on the wetting effect. Examples are shown in Figure 3e,f, where the synthesized cotton fabric and glass show hydrophobic properties. In addition to the wetting effect at room temperature, the wetting phenomenon has also been observed and applied at elevated temperatures (Figure 3g), such as soldering. Differing from the inert wetting at room temperature, phase reaction may take place at high temperatures. This is often known as reactive wetting (see refs. [68–70]).

The wetting effect shown in Figure 3 is controlled either by changing the surface chemistry or by varying the structure of the surface, known as chemically patterned substrate and mechanically patterned substrate, respectively. In the following, we define the chemically patterned surface as type C and mechanically pat-

terned substrate as type M. For example, the coating effect on the glass is achieved by changing the surface chemistry, which belongs to type C. The superhydrophobicity of the lotus leaf is due to the surface heterogeneity, classified as type M. In each classification, the wetting phenomenon is further sorted according to the ratio of the length scale of the droplet to the surface heterogeneity. According to the substrate type and the corresponding length scales, Table 1 lists some key investigations for the wetting effect of droplets on patterned substrates in bluepast 10 years, together with potential applications.

For type C substrate, most of the studies focused on the situation where the droplet size  $l_d$  is comparable to the chemical heterogeneity  $l_p$ . Typical references are refs. [71–85]. A brief summary of these works for  $l_d \sim l_p$  is as follows. Hartmann et al.<sup>[71]</sup> addressed the morphological transition of droplets on chemically stripped patterned surfaces by using sessile droplet experiments combined with simulations based on free energy minimization. Malijeviský et al.<sup>[72]</sup> studied fluid adsorption and bridging transitions at chemically stripped patterned surfaces using mesoscopic interfacial models and microscopic density functional theory. Russo et al.<sup>[73]</sup> used a volume-of-fluid method to study the outcome behaviors of droplets impacting similar patterned surfaces and successfully predicted droplet splitting and vectoring behaviors. Ewetola et al.<sup>[74]</sup> and Groves et al.<sup>[75]</sup> numerically investigated the motion and evaporation behaviors of a 2D droplet on chemically stripped patterned surfaces. Refs. [76–78] examined the wetting droplets on type C substrates via the lattice-Boltzmann method (LBM). In refs. [79–82], a phase-field approach in combination with an energy map method was utilized to identify different equilibrium shapes of droplets on type C substrates. Dević et al.<sup>[83]</sup> theoretically and numerically investigated the shape of nanodroplets with different volumes on an elliptical patch patterned substrate. Chowdhury et al.<sup>[84]</sup> simulated the transport and splitting of droplets on a Y-shaped wettability-gradient track surrounded by a superhydrophobic surface. Geng et al.<sup>[85]</sup> developed a bioinspired surface with wettability gradient for highly enhanced fog collection. There is a paucity of investigations for the wetting effect with droplet size much larger than the chemical heterogeneity on type C substrate. These works include a series of explorations for wetting on chemically stripped patterned surfaces via LBM<sup>[86–88]</sup> and experimental studies for wetting on polygonal patterns.<sup>[89]</sup>

For type M substrate, there are a few studies for the wetting effect with  $l_d \sim l_p$ . These works include refs. [90–99]. A compact summary of these works is as follows. Chen et al.<sup>[90]</sup> experimentally explained the Cassie–Wenzel wetting transition for droplets on pillar-patterned substrates. For both small length scales of droplets and pattern size, molecular dynamic simulation was adopted in refs. [91, 92]. Refs. [93, 94] theoretically addressed the wetting on groove-patterned surfaces based on geometrical arguments. Special surface patterns were designed in experiments to achieve directional liquid transport<sup>[95–97]</sup> and liquid repellence.<sup>[98]</sup> In particular, Li et al.<sup>[95]</sup> reported a new method of microscopic liquid transport based on a unique topological structure that allows for a rapid, directional, and long-distance transport of liquid. Ref. [96] designed biomimetic multicurvature structures to collect and transport water with extremely enhanced transport speed. Feng et al.<sup>[97]</sup> fabricated 3D biomimetic ratchets patterned substrates that allow directional

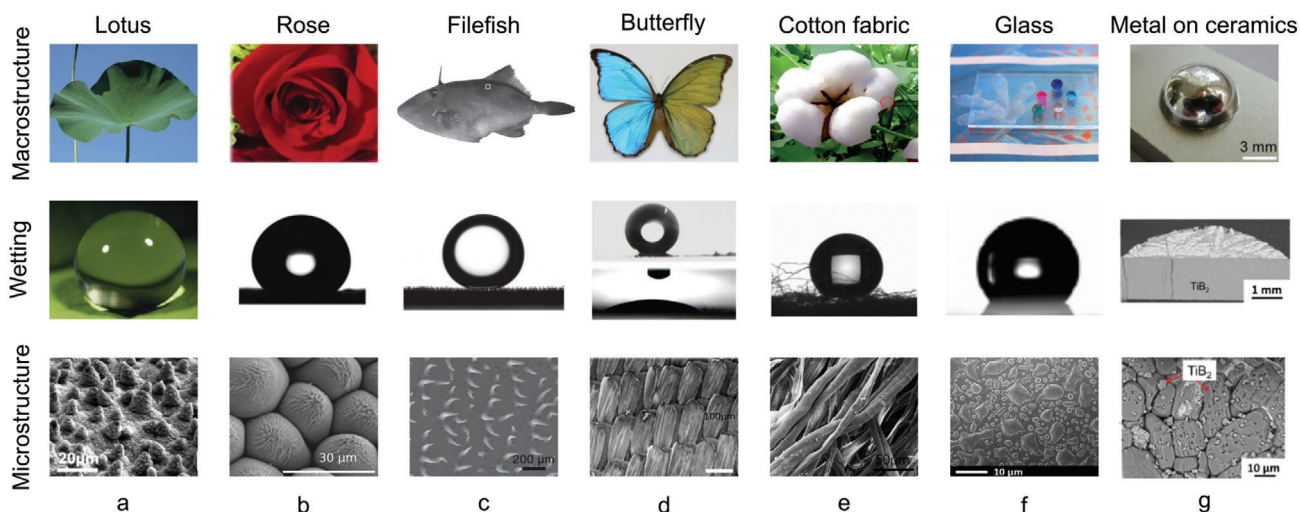


**Figure 2.** Wetting phenomena in nature, daily lives, and industrial applications classified as (top) macroscopic object, (middle) wetting morphologies, (bottom) microstructure of the surface. The droplet is water unless specified. a) Lotus leaf. Reproduced with permission.<sup>[54]</sup> Copyright 2009, Elsevier. b) Rose petal. Reproduced with permission.<sup>[55]</sup> Copyright 2019, Wiley-VCH. c) Filefish. Here, an oil droplet is placed in the surroundings of water for underwater applications. Reproduced with permission.<sup>[64]</sup> Copyright 2013, Wiley-VCH. d) Butterfly. Reproduced with permission.<sup>[18]</sup> Copyright 2019, American Chemical Society. e) Cotton fabric. Reproduced under the terms of the CC-BY Creative Commons Attribution 4.0 International license (<https://creativecommons.org/licenses/by/4.0>).<sup>[65]</sup> Copyright 2019, The Authors, published by MDPI. f) Coated glass. Reproduced with permission.<sup>[66]</sup> Copyright 2015, Elsevier. g) An alloy of Al–Ni droplets is placed on the top of TiB<sub>2</sub> ceramic materials at elevated temperatures greater than 700 °C. Reproduced with permission.<sup>[67]</sup> Copyright 2017, American Ceramic Society, published by John Wiley and Sons.

liquid transport based on the surface structure as well as the surface tension of the liquid. Lin et al.<sup>[98]</sup> utilized a functional surface with crater-like structures to largely reduce the integration of contact area over time; in this work, systematic investigations were conducted on the geometric parameters by many-body dissipative particle dynamics which provides guidelines for the design of water repellent surfaces. Most type M substrates have been

designed with micrometer and even nanometer scale structures, whose characteristic length  $l_p$  is much smaller than the droplet size  $l_d$ . Typical examples are shown in refs. [99–104]. For instance, Liu et al.<sup>[99]</sup> adopted a doubly reentrant structure that enables very low liquid–solid contact fraction which make the surface repel any liquid. This work reported a superomniphobic silica surface which can even withstand temperatures over 1000 °C

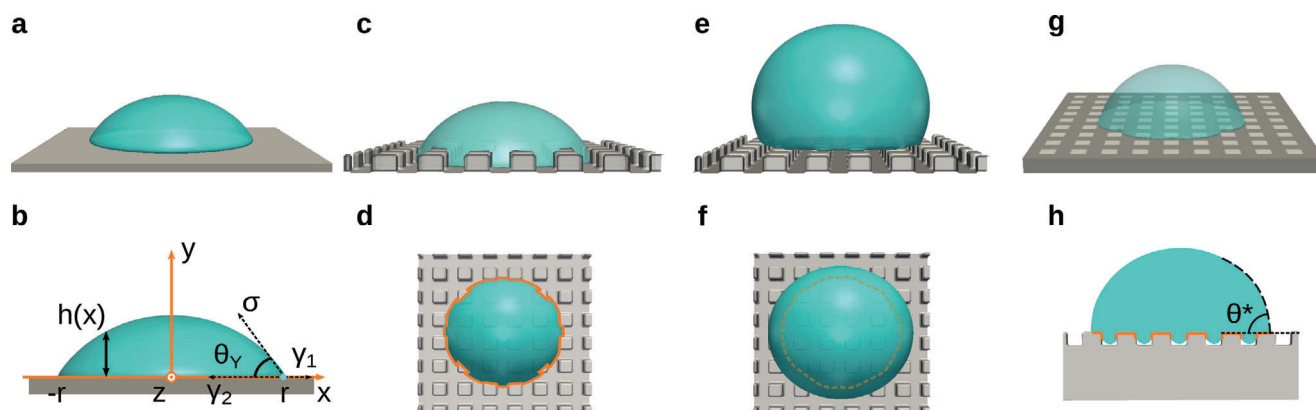


**Figure 3.** a–h) Sketch for Young's law on a homogeneous substrate (a,b) and the Cassie–Wenzel theory on mechanically and chemically patterned substrates (c–h). a) The wetting effect of a droplet (cyan) on a homogeneous solid substrate (gray). b) Vector notation for the Young's law, where the Young's contact angle  $\theta_Y$  is determined by the surface tension  $\sigma$  of the droplet–surroundings, and the difference of the interfacial energy densities between surroundings–substrate and liquid–substrate,  $\gamma_1 - \gamma_2$ . The cyan circle indicates the intersection T of the tangent lines of the solid–liquid interface, the liquid–surroundings interface, and the solid–surroundings interface. c,d) Schematics for the side and top views of the Wenzel wetting states, where the droplet completely penetrates into the gap between the pillars of the substrates (gray). e,f) Sketch for the side and top views of the Cassie wetting states, where the droplet stays over the gap between the pillars. g) Schematics for the wetting morphology on a chemically patterned substrate consisting of two different surface chemistries (dark and light gray). h) Schematic illustration for an intermediate wetting states, where the droplet partially penetrates into the gap between the pillars. The contact area between the liquid and the solid is used to estimate the effective wetting ratio  $f$  in ref. [63], as highlighted by the orange line.

**Table 1.** Summary of chemically and mechanically patterned substrates for the wetting effect.

References	Substrate and patterns	Scaling	Investigation methods and applications
[71–75]	Stripe pattern (C)	$l_d \sim l_p$	Theory/simulation/experiment; coatings for wear and corrosion protection, ink-jet printing, microcontact printing
[76–78]	Stripe/lattice patterns (C)	$l_d \sim l_p$	LBM/experiment; ink-jet printing, spray cooling, water harvesting
[79–82]	Stripe/lattice patterns (C)	$l_d \sim l_p$	Phase-field/theory; inkjet printing, spray cooling, coating, and microfluidic device
[83–85]	Elliptical patch/Y-junction shaped/wettability gradient patterns (C)	$l_d \sim l_p$	Theory/simulation/experiment, microfluidic devices, water harvesting
[86–88]	Stripe patterns (C)	$l_d \gg l_p$	LBM; smart surfaces for droplet manipulation
[89]	Polygonal patterns (C)	$l_d \gg l_p$	LBM/experiment; microfluidic chips
[90]	Pattern with pillars (M)	$l_d \approx l_p$	Experiment/theory; superhydrophobic surface
[91–94]	Pattern with pillars/groove (M)	$l_d \sim l_p$	Molecular dynamics/theory; self-cleaning surfaces, fiber coating and printing
[95–98]	Pattern with special structures (M)	$l_d \sim l_p$	Experiment/simulation; liquid diode, directional liquid transport, antifouling, functional surface
[99–104]	Pattern with nano-/microstructures (M)	$l_d \gg l_p$	Experiment; self-cleaning, biomimic surfaces, droplet-based microfluidic system, microreactors, drag reduction, antifogging, water harvesting
[105–108]	Patterns with pillars (M)	$l_d \gg l_p$	Experiment/theory; robust liquid repellent surfaces, bio-microarrays
[109–113]	Two-length scale pattern (M)	$l_d \gg l_p$	Theory/experiment; biomimic surfaces, self-cleaning topcoat for solar cells

Abbreviations: C/M, chemical/mechanical patterns; LBM, lattice Boltzmann method;  $l_d/l_p$ , droplet/pattern sizes.

and resist biofouling. Wang et al.<sup>[100]</sup> found water-repellent surfaces with high solid fraction nanoscale textures which is contrary to the Cassie–Wenzel theory. This can be explained by the fact that the line tension on the nanotextures and the compact arrangement of the nanotextures contribute to withstand the impact pressure of drops. This work is of great significance for designing robust water-repellent materials. Sun et al.<sup>[101]</sup> developed a biomimetic surface and the substrate surface was constructed by a special nanoparticles-dispersed phase which enables favorable hydrophobic property under selective fluorosilane decoration. Based on the photothermal effect of the substrate, the droplet wetting behaviors can be controlled. Lv et al.<sup>[102]</sup> experimentally examined in situ liquid–air interfaces on a submerged cylindrical microcavity-patterned surface. The transition from metastable states to the Wenzel state under different ambient pressure was quantified with a diffusion-based model. A similarity law along with a characteristic time scale was derived to predict the lifetime of the air pockets. This result has potential application for the drag reduction of submerged surfaces. Xu et al.<sup>[103]</sup> investigated the droplet spreading and wetting transition on the microcavity-patterned substrate. This work showed that the mesoscopic sequential Cassie–Wenzel transition leads to the macroscopic inward wetting transition from the periphery to the droplet center. A semiquantitative functional relationship between the sagging depth of meniscus in the microcavities and the droplet spreading velocity was given, which clarifies the mechanism for the wetting transition on microcavity-patterned surfaces. Kim et al.<sup>[104]</sup> observed that a high-speed impacting drop exhibits multiple nucleating holes triggered by microstructures of biological surfaces. This leads to the rapid retraction of the spreading drop and a decrease in contact time; the findings revealed the biological advantages for the reduction of hypothermia risk of animals.

Refs. [105–108]<sup>[105]</sup> studied the pillared patterns with experiments and theories. Two similar examples are ref. [105] and ref. [106]. Raj et al.<sup>[105]</sup> designed the substrates with structured chemical heterogeneity to tailor polygonal droplet contact area ranging from squares, rectangles, hexagons, octagons, to dodecagons. Most recently, Lou et al.<sup>[106]</sup> observed the formation of water and liquid metal polygonal droplets on non-wetting pillar patterned surfaces. Under the guidance of the Cassie–Baxter model and inspired by the lotus effect, Refs. [109–113] studied the two-length scale patterns. For example, Murakami et al.<sup>[109]</sup> addressed the Cassie–Wenzel transition on nano- or microscale hexagonal pillared surfaces. Dia et al.<sup>[110]</sup> presented a hydrophilic directional slippery rough surface which collects and removes water due to oil infused nanotextures upon directional microgrooves. Yun et al.<sup>[111]</sup> fabricated a springtail-inspired surface hierarchical system consisting of serif-T-shaped nanostructures on microscale wrinkles displaying both high static repellency and pressure resistance. The fabricated surface shows high repellency to diverse liquids and can endure extreme pressure resulting from the impacting drops. Nagayama et al.<sup>[112]</sup> studied the porous/patterned silicon substrates and noticed the limitation of the Wenzel and Cassie–Baxter model and proposed a partial wetting model to describe the diverse intermediate wetting states. Wang et al.<sup>[113]</sup> designed a special two-length scale pattern to increase the mechanical robustness of the superhydrophobic surfaces.

Potential applications of type C and type M substrates are exemplarily listed in Table 1. When  $l_d \sim l_p$ , both type substrates are well used for droplet manipulations and directional transport of liquid, such as inkjet printing, microelectronics, and microfluidic devices. In the case  $l_d \sim l_p$ , the shape and the movement of the droplet are more controllable comparing with the situation  $l_d \gg l_p$  where more uncertainties appear, such as roughness. When

$l_d \gg l_p$ , type M substrate is often applied for biomimic functional surfaces, as inspired by the power of nature, such as the leaf of the lotus, wing of the butterfly, skin of the filefish, back of Namib desert beetle, and feathers of the kingfisher. These bio-inspired functional surfaces are typically applied for self-cleaning and liquid-repellency. When  $l_d \gg l_p$ , type C substrate is usually used for coating and micropatterned surfaces which have the functionalities of anti-fogging and anti-fouling.

In the past decade, the study of wetting effect on patterned substrates started with the simple stripped surfaces and then focused on more complex 2D and 3D patterned substrates. These investigations lead to more deep understandings on the wetting mechanism, giving rise to novel designs of functional substrates; but also engendering diverse unexplored phenomena. In this report, we will overview recent progresses for the design of patterned substrates based on the Cassie–Wenzel theory. Two key parameters for the materials design according to the Cassie’s equation are the intrinsic Young’s contact angle and the contact area between the droplet and the solid substrate. Thereafter, some limitations of the Cassie–Wenzel theory will be discussed. When the droplet size is comparable with the surface heterogeneity, the Cassie–Wenzel theory loses its validity and anisotropic wetting morphologies often appear. In this case, the anisotropic wetting morphologies depend on the shape, orientation, and arrangement of the surface heterogeneity, the droplet volume, the deposition position of the liquid, and the kinetics. Recent advances for the surface design within the scope of these impact factors will be elucidated in the following. At the end, we will conclude the present report with a thermodynamic interpretation of the wetting effect and the corresponding open questions.

## 2. Cassie–Wenzel Theory and Its Limitation

### 2.1. Notations

In the scientific community of the wetting effect, many notations and phrases have been used to describe this phenomenon, such as contact angle, apparent contact angle, mechanically/chemically patterned substrate, etc. In order to be consistent with literature, we state commonly used phrases and notations for the wetting effect following ref. [114]. The triple junction T is the intersection of the tangent lines of the solid–liquid interface, the liquid–surroundings interface, and the solid–surroundings interface, as sketched in Figure 2b. The contact angle  $\theta$  is defined as the angle between the tangent lines of the solid–liquid and liquid–surroundings interfaces inside the droplet. When the substrate  $S$  is a pure substance solid phase and has a uniform normal vector, that is,  $\mathbf{n}(\mathbf{x}) = (0, 1, 0), \forall \mathbf{x} \in S$ , the contact angle is named as Young’s contact angle  $\theta_Y$  for a static droplet; before reaching the static state, the contact angle is the dynamic contact angle which may change with time  $t$ . The system with a pure substance substrate without roughness/defect is said to hydrophobic and hydrophilic, when  $\theta_Y > 90^\circ$  and  $\theta_Y < 90^\circ$ , respectively. The special case of  $\theta_Y = 90^\circ$  is called as the neutral state. When the substrate is rough (see Figure 2c,e), the normal vector is non-uniform on the substrate. Referring to the triple junction according to the local normal vectors and the respective tangent lines, we have local Young’s contact angle for a static droplet and local dynamical contact angle when the droplet

moves with respect to the substrate/the surroundings. The local Young’s contact angle is sometimes known as intrinsic Young’s contact angle. The local Young’s contact angle can deviate from the apparent contact angle on a rough surface. When the droplet is in static on a roughness surface, the apparent contact angle is usually addressed by the intersection of two curves: one curve is the droplet–surrounding arc fitted by a circle and the other curve is the connection line for the envelopes of the roughness pillar. The intersection of the connection curve with the circle defines the apparent contact angle, as sketched in Figure 2h and denoted by  $\theta^*$ . Here, only one length scale of the pillar is considered. This definition loses its validity when the surface has multiscale roughness, such as lotus leaf, and may be used by considering the surface pillar of the largest scale to depict the apparent contact angle. The hydrophilicity and the hydrophobicity of the system with a roughness surface are according to the value of  $\theta^*$ , contrary to the intrinsic hydrophilicity/hydrophobicity based on  $\theta_Y$ . The advancing  $\theta_A$  and receding  $\theta_R$  contact angles are the maximum and minimum values of  $\theta^*$ , respectively. A smooth substrate refers to a pure substance surface without roughness/defect. The mechanically patterned substrate is defined when the normal vector is non-uniform on the substance. The chemically patterned substrate is defined when the substrate has more than one substance. The characteristics of the mechanically and chemically patterned substrates are the normal vector  $\mathbf{n}$  and the wall energy, respectively, which will be discussed in Section 6.

For the wetting effect on heterogeneous substrate, a concept of thermodynamic contact angle has been introduced after the work of Tadmor.<sup>[115]</sup> This work has been recently discussed in ref. [116] and may be related to “the most stable contact angle” stated in ref. [117]. Because of the surface irregularities, a variation of the energy density,  $\mathcal{K}d\mathcal{L}$  with the unit of  $\text{J m}^{-2}$  is added to account for the modification of the apparent contact angle. Here,  $d\mathcal{L}$  is the infinitesimal element of the deformed contact line and thus  $\mathcal{K}$  has a unit of  $\text{J m}^{-1}$ , which is called as line energy density. As derived in ref. [115], the line energy density  $\mathcal{K}$  depends on the droplet volume as  $\mathcal{K} \propto V^{1/3}$ . With the assumption that the absolute values of the line energy density are the same for advancing and receding, one derives a thermodynamic contact angle. This concept provides a way to calculate the Young’s contact angle according to the apparent contact angle on heterogeneous substrate.

### 2.2. Cassie–Wenzel Theory

From Young’s law, the apparent contact angle  $\theta^*$  of a droplet on a homogeneous solid substrate (Figure 2a) is related to the energy density  $E$  creating the solid–liquid contact area and the surface tension  $\sigma$  of the droplet as  $\cos\theta^* = -E/\sigma$ , where  $E = \gamma_2 - \gamma_1$ , with  $\gamma_1, \gamma_2$  being the interfacial energy densities of solid–gas and liquid–gas, respectively. The Young’s law is often interpreted by a vector notation, as sketched in Figure 2b. At the triple junction, the three surface-tension forces  $\sigma, \gamma_1$ , and  $\gamma_2$  are in the tangential direction of the droplet, along the solid–liquid interface, and along the solid–gas interface, respectively. The balance of these three surface tension forces in the dimension parallel to the surface of the substrate yields the Young’s equation. This elegant interpretation is consistent with the thermodynamic consideration of energy minimization. By calculating the total energy

$F$  with contribution from liquid–gas, solid–liquid, solid–gas, we obtain  $F(\theta)$  as a function of  $\theta$  (or the base radius  $r$ ). The Young’s law is achieved by addressing  $F'(\theta) = 0$ .<sup>[118]</sup> Here, an assumption is made that the liquid–gas interface is a spherical cap. This assumption is reasonable since the spherical geometry has the least specific surface area.

When the substrate is mechanically heterogeneous, the vector interpretation yields no answer, since to the effects of roughness, the directions of the “surface tension vectors” are not well defined within infinitesimally small distance from the triple interface. Moreover, the vector interpretation has to be applied both at the heterogeneity of the triple junction and at other heterogeneities beneath the droplet away from the triple junction. For a solid substrate with  $N$ -heterogeneity which can be either chemical or mechanical, the energy density to create the base area of the droplet is  $E = \sum_{i=1}^N E_i f_i$ , where  $f_i$  represents the area fraction of the  $i$ th heterogeneity covering by the droplet satisfying  $\sum_{i=1}^N f_i \approx 1$ . Through the way analog to the Young’s law, we arrive the classic Cassie–Wenzel equation

$$\cos \theta^* = \sum_{i=1}^N f_i \cos \theta_{Y_i} \quad (1)$$

where  $\theta_{Y_i}$  is the intrinsic Young’s contact angle on the  $i$ -heterogeneity. When  $N = 1$  and  $f_1 = 1$  indicating a smooth substrate, we have the classic Young’s law; when  $N = 2$  and  $f_2 = 0$ , we obtain Wenzel’s equation with  $f_1$  being the real contact area of the solid–liquid interface which may be called as the roughness factor; when  $N = 2$  and  $\theta_{Y_2} = 180^\circ$ , the Cassie’s equation  $\cos \theta^* = f_1 (\cos \theta_{Y_1} + 1) - 1$  is replicated for porous structure with porosity  $f_2 \approx 1 - f_1$ . The setup of  $\theta_{Y_2} = 180^\circ$  indicates a contact of the droplet with air. From Cassie’s equation, the wettability of the system depends on two parameters: the intrinsic Young’s contact angle  $\theta_Y$  and the solid–liquid contact area fraction  $f_1$ . Based on this understanding, a hydrophilic material with  $\theta_Y < 90^\circ$  can be hydrophobic if we reduce the contact area  $f_1$ . For instance, when  $f_1$  is relatively small, we have  $\cos \theta^* \approx -1$  and obtain a superhydrophobic structure  $\theta^* \approx 180^\circ$ . This is mostly the underlying mechanism for the superhydrophobic property of lotus/rose leaves<sup>[119]</sup> and many other plants in nature.<sup>[6,120]</sup> In fact, the lotus leaf has many microscale bumps and numerous nanometer hair-like apophysis on each microbump,<sup>[121]</sup> enabling to decrease the solid–liquid contact area. This kind of two length-scale structure has also been observed on the wings of butterfly<sup>[122]</sup> and many other insects,<sup>[123]</sup> which exhibit superhydrophobicity. Benefiting from the Cassie’s theory, superhydrophobic materials can be designed from a hydrophilic substrate. Some recent progresses of this design based on Cassie’s theory will be overviewed in the following.

The Young’s law and the Cassie–Wenzel theory have also been derived by other methods. A variational framework has been proposed in ref. [124]. In this work, by assuming that the droplet is axisymmetric and that each cross-section of the droplet is a part of a circle with a base radius  $r$  (Figure 2b), the total free energy of the droplet is calculated as

$$\mathcal{G}(r) = \int_0^r \left[ 2\pi\sigma x \sqrt{1 + (h')^2} + 2\pi x E \right] dx \quad (2)$$

where  $h(x)$  is the height of the cross-sectional droplet–gas interface referring to the solid surface at each position  $x$  ranging from the base center  $x = 0$  to  $x = r$ . The first part in Equation (2) is the energy contribution from the droplet cap. The second part in Equation (2) results from the contact between the liquid and the solid. For the formulation of the energy density  $E$ , there are three different cases: i) Young’s case,  $E = \gamma_2 - \gamma_1$ ; ii) Wenzel’s case,  $E = (\gamma_2 - \gamma_1)r_w$ , where  $r_w$  is the roughness factor and corrects the solid–liquid interface energy density from  $(\gamma_2 - \gamma_1)$  due to the roughness; and iii) Cassie’s case,  $E = \sum_{i=1}^N f_i E_i$ . By minimizing the free energy  $\mathcal{G}$  via  $\mathcal{G}'(r) = 0$  subjected to the volume constraint  $V = \text{const}$ , we obtain the Young’s and the Cassie–Wenzel equations. Another derivation for the Young’s law and the Cassie–Wenzel theory is shown in ref. [125], which is based on the maximum entropy principle that is equivalent to the free energy minimization for an isothermal consideration. Differing from the volume constraint in ref. [124], a geometrical constraint based on the Gauss–Bonnet theorem is adopted for the free energy minimization in ref. [125]. In this theorem, the Euler characteristic  $\chi$  is related to the Gauss curvature  $\int_A \kappa_G dA$  along the cap surface of the droplet  $A$  and the deficit curvature  $\kappa_d$ . By using this constraint, the minimization of the free energy results in the Young’s law and the Cassie–Wenzel theory.

The popularity of the Cassie–Wenzel theory lies its feasibility for an intuitive understanding and indeed, this quintessential theory shows its functionality quite well in some cases. However, there are some shortcomings of this classic theory. Two reasons are listed here: i) In the derivation for the Cassie–Wenzel equations, the contact area of a curved liquid–gas interface inside the pore for a non-smooth substrate is overlooked. In the Wenzel model, there is no contact between liquid and gas inside the pore; the liquid completely contacts the solid substrate inside the pore and the real solid–liquid contact area is corrected by the roughness factor  $r_w$ . In the Cassie model, the liquid does not penetrate into the pore at all and the liquid–gas interface between two adjacent pillars is assumed to be flat. The liquid–solid and liquid–gas contact areas on the surface are calculated according to the porosity of the substrate. However, in real cases, the liquid can partially penetrate into the pore, forming a curved liquid–gas interface between two neighboring pillars, as sketched in Figure 2h. In this case, the real contact areas between the solid and the liquid and between the liquid and the trapped beneath air in the pore are extremely challenging to be measured. The real contact area is affected by the shape as well as the arrangement of the mechanical heterogeneity. Noteworthy, the summation of the contact area fraction of different heterogeneities is not necessarily to be unity. The summation is close to unity only when the droplet is large enough so that the base area of each heterogeneity covering by the droplet is in accordance with the global area fraction  $f_i$  according to the statistical probability. That is, the chance of the triple line meeting the  $i$ th heterogeneity is  $f_i$  when the droplet diameter is much larger than the characteristic length of the heterogeneity. ii) It has been assumed that the liquid–gas cap has a spherical shape, which is axisymmetric. This postulation is not necessary to be an axiom. In Young’s law where a smooth substrate is considered, the assumption of a spherical liquid–gas cap is reasonable because the spherical geometry has the least specific surface area. But surface heterogeneities can destroy the symmetry of the liquid–gas cap, leading to an irregular

and non-spherical liquid–gas cap. The energy minimization should take the real shape of the liquid–gas cap as well as the energy density of the curved base area  $E = \sum_{i=1}^N f_i E_i$  into account. A consideration of the two facts (i) and (ii) can lead to numerous other energy barriers beyond the scope of the Cassie–Wenzel theory, engendering many other metastable states. An intermediate state between the Cassie and the Wenzel states is sketched in Figure 2h. The new energy barriers out of the context of the Cassie–Wenzel prediction open a Pandora’s box, providing immense opportunities for designing substrates with different extraordinary functions but indeed being challenging to be controlled. We believe this is one of the most important reasons for so much effort having been devoted by scientists to the wetting topics and to the design of functional substrates in recent decades; these enormous efforts are still being made. Moreover, the new energy barriers depend on the droplet volume, the shape of the heterogeneity, the arrangement of the heterogeneity, the dimension of the heterogeneity. For instance, the lotus leaf has a microscale bumps and nanometer-scale hair-like structures; the dual length-scale topography affects the contact line kinetics by lowering the energy barrier between metastable states.<sup>[126]</sup> These metastable states are challenging to be depicted by the Cassie–Wenzel theory. In view of the masterpiece work of Cassie–Wenzel as well as the possibility of many other metastable states differing from the Cassie/Wenzel states, we will overview some recent progresses on the wetting effect on patterned substrate and some novel developments for the design of functional substrates.

### 2.3. Review Articles in Recent Years from 2020–2022

Many review papers have been devoted to the wetting effect on patterned substrate. We classify these review papers as theory in the way of “thinking and predicting” and applications in the way of “doing and realizing.” For theories, recent discussions have been focused on the pinning retention force along the three-phase contact line. Two comprehensive reviews for this topic are refs. [127, 128]. In ref. [128], different theories for the droplet pinning on patterned substrate are presented. These theories include the work of Thomas Young,<sup>[51]</sup> Cassie–Wenzel,<sup>[52,53]</sup> Huh and Mason,<sup>[129]</sup> Marmur,<sup>[130]</sup> de-Gennes–Brochard–Wyart–Quéré–Joanny,<sup>[1]</sup> Furmidge–Kawasaki,<sup>[131,132]</sup> Extrand–Gent<sup>[133]</sup> and Tadmor.<sup>[134–136]</sup> The first two theories have already been overviewed in Section 2.2. In Huh and Mason’s discussion, it is assumed that the surface has periodic peaks and pits for a chemically homogeneous substrate. With this assumption, the apparent contact angle varies periodically in space. This is used to explain the variation of the apparent contact angle with the position of the contact line with respect to the peaks and pits. In Marmur’s approach, it is assumed that the local Young’s contact angle varies periodically in space, which might be due to chemical heterogeneity. Thus, the receding and advancing contact angles are different values from the local Young’s contact angle in space when the contact line reaches different positions. In the consideration of de-Gennes–Brochard–Wyart–Quéré–Joanny, the surface is proposed to have chemical blemishes, which modify the local energy density between solid–liquid and solid–gas, leading to a new apparent contact angle differing from the non-defect surface. By this way, the apparent contact angle depends on the

size of the chemical defects and can be greater or less than the Young’s contact angle on the non-defect surface. The work of de-Gennes–Brochard–Wyart–Quéré–Joanny leads to a difference in the receding and advancing contact angles relating to a characteristic length “provided by some macroscopic sample size.” By considering a droplet on a tilt surface, the difference between the receding and advancing contact angles has been depicted by the Furmidge–Kawasaki equation and Extrand–Gent. The difference of the results between Furmidge–Kawasaki and Extrand–Gent is the prefactor  $k$  for  $k(\cos\theta_R - \cos\theta_A)$ . Alternative way of bottom-up thinking is the work of Tadmor from the microscopic scale to the macroscopic level. In the theory of Tadmor, it is postulated that the solid–liquid interaction is modified after depositing the liquid on the solid substrate. In the microscopic scale, the solid molecules reorient at the triple line, which changes the interfacial energies and thus the apparent contact angle. The variation of the interfacial energies leads to the pinning effect. The advantages and disadvantages of each model have been systematically discussed in ref. [128].

Another recent discussion for the droplet retention force is reviewed in ref. [127]. The estimation for the droplet retention force is based on the work of Reyssat and Quéré.<sup>[137]</sup> By considering a pillar-structured surface, the retention force per unit length of the droplet boundary is expressed as

$$f_{re} = \frac{1}{8\pi} \sigma \mathcal{A} \delta_m^2 \ln \frac{2\pi}{\delta_m} \quad (3)$$

where  $\delta_m$  is the top perimeter normalized by the pitch and  $\mathcal{A}$  is an empirical value accounting for the curved liquid–gas interface that is overlooked in the Cassie–Wenzel theory. For the calculation of  $\delta_m = l/\lambda$ , the length of the effective contact line  $l$  on a unit pattern and the periodicity of the pattern  $\lambda$  should be given. A constant value  $\mathcal{A}$  and  $\delta_m$ , leads to a constant force per unit length, which seems to be consistent with work of ref. [138]. The challenging point here is that the effective length of the contact line is unknown. The value of  $\mathcal{A}$  and  $\delta_m$  may be related to the effective wetting ratio  $f$ , as introduced in ref. [63] and will be discussed in Section 4.

Recent experiments from 2019 to 2021 for sessile droplet wetting on structured surface have been overviewed in ref. [139]. A main conclusion here is that most experiments show a 2D view of the wetting morphology and that the apparent contact angle should be measured in 3D with sectional views in different directions. In 3D, the three-phase contact line could be a non-circular shape. Specially, when the droplet size is comparable with the substrate pattern size, non-circular shape of the contact line occurs and the effect of the ratio of the droplet size to the substrate pattern size shall be further studied. A review for this direction will be provided in Section 5. In addition, the evaporation and condensation effects on the wetting on patterned substrates are discussed in ref. [139] for the formation of irregular droplet shape and non-circular three-phase contact line. For the effect of evaporation and condensation to the wetting phenomenon on patterned substrate, we refer to refs. [140–144].

Review works for the application of the wetting effect on patterned surface have been provided in refs. [45, 145, 146]. In ref. [146], the focus is on the droplet manipulation, such as droplet isolation, droplet dynamics, and droplet patterning, via

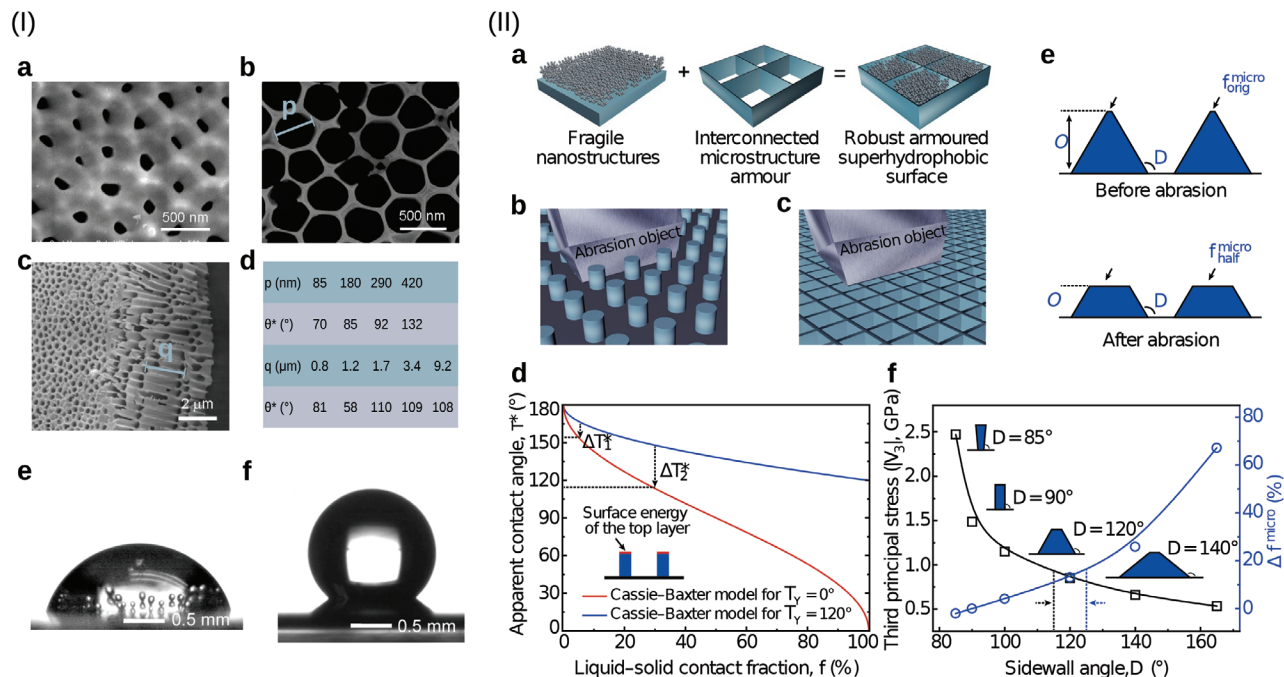


**Figure 4.** Experimental corroboration of the Cassie–Wenzel theory<sup>[153]</sup> and design of robust superhydrophobic substrates.<sup>[113]</sup> Panel I: Wetting effect on porous alumina with different pore size. a,b) Top view of porous alumina with pore diameters of 85 nm and 420 nm, respectively. c) Side view of porous alumina with a depth of 9.2  $\mu\text{m}$  and a pore diameter of 400 nm. d) The apparent contact angle  $\theta^*$  for a 3  $\mu\text{L}$  water droplet deposited on the porous alumina as a function of the pore diameter  $p$  and pillar depth  $q$  of the microstructure. In the former and the latter cases, the pillar depth and the pore diameter are fixed at 4.5  $\mu\text{m}$  and 400 nm, respectively. I) Reproduced with permission.<sup>[153]</sup> Copyright 2008, American Chemical Society. Panel II: Design of a robust superhydrophobic surfaces based on the Cassie–Wenzel theory. a) Sketch for enhancing the mechanical stability of the fragile nanostructures with adding a protective microstructure “armor.” b) The abrading object can easily insert in between the discrete microstructures, damaging both the nanostructure and the microstructure. c) Abrasion objects that are larger than the armor frame are blocked by the microstructure. d) The apparent contact angle  $\theta^*$  versus the liquid–solid contact area fraction  $f$  according to Cassie’s equation for two different  $\theta_Y$ . e) The change of the contact area on the top of the microstructure when the height is fractured to half of its original value by abrasion. f) Effect of the sidewall angle  $\alpha$  on the mechanical stability and the liquid–solid contact area fraction  $\Delta f_{\text{micro}}$ . II) Reproduced with permission.<sup>[113]</sup> Copyright 2020, Springer Nature.

designing particular artificial surface heterogeneities. It has been pointed out in ref. [146] that the robustness of the heterogeneous wettability is a great challenge. In Section 3, we will present a recent work which fabricates highly robust superhydrophobic metals, glass, and ceramics. In ref. [145], the application for the wettability materials is presented for biomedical engineering, such as tissue engineering, biosensing, and serving as medical devices. The manipulation of the wettability is achieved by changing the surface topology and chemical composition, which has also been overviewed in ref. [45]. Both the designs in ref. [145] and in ref. [45] are based on Young’s law and Cassie–Wenzel theory.

With these summaries, we see that there is a paucity of review work for the wetting effect when the droplet size is compared to the pattern size. The present review has three folds: i) The design of artificial surface based on the Cassie–Wenzel theory. In particular, design for the robustness of wettability substrate is discussed. ii) The extension of the Cassie–Wenzel theory to a partial wetting model, where the curved liquid–gas interface in the pore on mechanically patterned substrate is considered. iii) When the droplet size is not far greater than the surface heterogeneity, the Cassie–Wenzel loses its validity and anisotropic wetting shapes appear, which is a special feature of this review including theory, numerical simulation, and experiments. Last but not the least, we will present a thermodynamic interpretation of the wetting effect on patterned substrate, which is consistent

with previous theories. Noteworthy, the present work focuses on quasi-equilibrium wetting states, which is mostly the consideration in aforementioned reviews. At the end, we will also point out that the kinetic energy due to the Kortweg stress should be considered for the energy minimization when the droplet is moving. This is essentially important for drop impact, which is out of the scope of this work. We refer to refs. [147–152] for droplet impact and bouncing.

### 3. Design of Functional Substrates according to the Cassie–Wenzel Theory

As mentioned in Section 2, the apparent contact angle  $\theta^*$  of a droplet on a mechanically patterned substrate depends on the intrinsic Young’s contact angle  $\theta_Y$  and the liquid–solid contact area fraction  $f$ . By manipulating these two factors, the wettability of the system is controllable. In this section, we overview some recent efforts in designing functional surfaces via changing  $f$  and  $\theta_Y$  based on the Cassie–Wenzel theory.

Figure 4I shows an experimental corroboration for the transition from the Wenzel state to the Cassie state on a substrate of porous alumina with different pore sizes. In this experiment, a water droplet of 3  $\mu\text{L}$  is placed on top of the porous alumina, whose Young’s contact angle on a smooth alumina is 85°. When the pore diameter is about 85 nm (Figure 4I(a)) corresponding

to a relatively large contact area between the droplet and the substrate, the apparent contact angle is  $\approx 70^\circ$ , less than the Young's contact angle. The wetting morphology is shown in Figure 4I(e). An increase in the pore diameter to 420 nm (Figure 4I(b)) indicating a decrease in the contact area results in an apparent contact angle of  $140^\circ$ , as depicted in Figure 4I(f). The transition from hydrophilicity to hydrophobicity is in accordance with Cassie's equation. The variation of the apparent contact angle as a function of the pore diameter is summarized in Figure 4I(d). The experimentally measured apparent contact angle has been qualitatively compared with the Cassie–Wenzel equation. By using the area fraction of 0.21 for the pore diameter of 420 nm, the Cassie angle is  $140^\circ$ , which shows good agreement with the experimental value of  $132^\circ$ . For the pore diameter of 85 nm, the roughness factor is 6.8. With the Young's contact angle of  $85^\circ$ , the Wenzel angle is  $54^\circ$ , which deviates from the experimental value of  $70^\circ$ . This deviation is attributed to the air pockets trapped underneath the water. The Wenzel state cannot be fully replicated because of the trapped air in the gap, which is not completely excluded but compressed, proving additional force for establishing metastable states between the Cassie and Wenzel states. The experiments have been further analyzed by varying the depth of the pillar; a side view of the pillar for the porous alumina microstructure is illustrated in Figure 4I(c). For a small depth, the air in the gap is expelled easily. In this case, one observes an apparent contact angle preferring the Wenzel state or near Wenzel state. For a large depth, the air in the gap has an upward force contribution against the penetration of the droplet into the pore, leading to a large apparent contact angle. The experimental observation for the variation of the apparent contact angle with the depth is summarized in Figure 4I(d). The non-monotonic evolution of the contact with the pillar depth shows the complexity of the Cassie–Wenzel transition. To obtain a more quantitative analysis, one should investigate the penetration of the droplet within the context of two length scales. One is the pore scale considering the pressure due to the curvature of the liquid–gas interface as well as the state equation of the gas. If the volume of the droplet is sufficiently large, the gravitation force is comparable with the Young–Laplace pressure force and should be considered for the force balance inside the pore. The other one is the macroscopic scale, where the droplet–air interface has a non-zero curvature, which results in the Young–Laplace pressure of the droplet at static. A stable wetting state is established if the pressures at the pore scale and at the macroscopic level are identical. This kind of analysis is known to be the pressure model in literature.<sup>[154,155]</sup>

External force may be introduced to induce the Cassie–Wenzel transition, as discussed in refs. [138, 156]. Two different methods are used in literature for this purpose. In the first way, the droplet volume is varied, which changes the body force of the gravity and therefore modifies the gravitational pressure on the surface. By this way, the apparent contact angle decreases with the droplet volume. In the second approach, the droplet is pressed by applying a solid substrate on the top of the droplet. With an increase in the force exerted on the substrate above the droplet, the apparent contact angle decreases. Both approaches indicate the penetration of the liquid into the pore and the evolution of the droplet toward the Wenzel state to achieve a complete contact between the solid and the liquid. Motivated by the second approach, a vi-

brating droplet method has been adopted in ref. [138] to examine whether the transition from Cassie to Wenzel states is a 1D or 2D affair. In this method, a vertical vibration force is applied and the pressure resulting from the inertial force due to vibration is summed with the pressure resulting from the mean curvature and the gravity. The result shows that the total pressure multiplying by the radius of the droplet is almost a constant. Based on this result, it is suggested that the threshold for the Cassie–Wenzel transition is a force acting on the unit length of a triple line ( $\text{N m}^{-1}$ ) rather than the pressure ( $\text{N m}^{-2}$ ). The present authors suggest more discussions for the state of the air trapped in the pocket during the Cassie–Wenzel transition. The air pressure in the air pocket increases when the volume is reduced if the air is compressed according to the van der Waals equation for ideal gas and works against with the external force applied on the droplet. The air can also dissolve into the liquid, forming gas bubbles. The curvature pressure at the interface of the liquid–air cap and in the air pocket no longer follows the Young–Laplace description when the interface deviates from a spherical cap if the gravity effect comes into play.<sup>[157]</sup> In addition, the capillary force along the triple line of liquid–solid–air in the air pocket should be considered. In contrast to the consideration of the force balance, the energy minimization approach (see refs. [63, 118]) seems to be more appropriate to address the metastable states between the Cassie and Wenzel states and the transition between these two states, although force balance and energy minimization represent the same physics. In particular, the Cassie state, the Wenzel state, and the Young's equation have been derived by the energy minimization approach.<sup>[118]</sup> This method has not yet been applied when the liquid–air interface is curved in the air pocket. By assuming an effective wetting ratio  $f$  (Figure 2h) for a curved liquid–gas interface in the air pocket, intermediate states have been estimated based on the energy minimization, as will be discussed in Section 4.

In real applications, the pillars of the mechanical patterns could be abraded when in contact with other solid materials. In this case, the solid–liquid contact area increases, reducing the wettability according to Cassie's equation. Other factors which may affect the contact area is oxidation,<sup>[158]</sup> corrosion,<sup>[159]</sup> etc. From the aspect of enhancing hydrophobicity, the contact area should be reduced; however, a low contact area normally leads to a fragile surface, which can easily be abraded. By considering a compromise of wettability and mechanical stability, a robust superhydrophobic surface has been designed by Wang et al.<sup>[113]</sup> Figure 4II illustrates a specially structured surface designed in ref. [113], which realizes great improvements in the robustness of the superhydrophobicity. This surface has two-length scale, namely, a fragile nanostructure providing water repellency and a microstructure providing long-time durability. Figure 4II(b,c) compares the abrasion mechanisms for the damages of the discrete (normal design) and interconnected microstructures (the current novel design), respectively. In Figure 4II(b), the abrading objects are accessible between the microstructures and thus can easily destroy both the microstructures and nanostructures, whereas in Figure 4II(c), abrasives larger than the size of the interconnected microstructure frames are blocked. By this design, the nanostructures can be protected from being removed by relatively large abrasives due to the sieve effect of the microstructure frames. Figure 4II(d) shows the apparent contact

angle  $\theta^*$  as a function of liquid–solid contact area fraction  $f$  for given intrinsic Young's contact angles  $\theta_Y = 0^\circ$  and  $\theta_Y = 120^\circ$ , as presented by the red and blue curves, respectively. The difference between the two curves decreases with decreasing  $f$ , revealing a less important effect of surface chemistry on the system wettability for a small liquid–solid contact area fraction. The hydrophobicity can be guaranteed by keeping small  $f$  even if the original hydrophobic surface is abraded. In addition, with a dedicated design of the geometry (e.g., adjusting the sidewall angle  $\alpha$ ), the interconnected frames can strengthen the mechanical robustness of the surfaces, as demonstrated by the finite-element simulation. By varying  $\alpha$  while keeping the top contact area of the microstructures constant, the stress distributions for these microstructures under a fixed load are simulated. As shown in Figure 4II(f), the third principal stress ( $|\sigma_3|$ ) reduces as  $\alpha$  increases (black curve), proving the improvement for the stability of the microstructures for large  $\alpha$ . However, the increase of  $\alpha$  leads to an enlargement in the liquid–solid contact area, which is characterized by  $\Delta f^{\text{micro}} = f_{\text{half}}^{\text{micro}} - f_{\text{orig}}^{\text{micro}}$ . Here,  $f_{\text{orig}}^{\text{micro}}$  and  $f_{\text{half}}^{\text{micro}}$  denotes the liquid–solid contact fraction for the original microstructures and when half of the height is abraded, respectively (Figure 4II(e)). The mechanical stability requires large  $\alpha$ , while superhydrophobicity needs small  $\alpha$ . The final design criterion for this functional surface is a compromise between the superhydrophobicity and the mechanical stability, as highlighted in Figure 4II(f) where  $\alpha$  around  $120^\circ$  is preferred. Note that the real liquid–solid contact fraction depends not only on the microstructures but also on the nanostructures according to the Cassie equation:

$$\cos \theta^* = f^{\text{micro}} (\cos \theta_Y^{\text{micro}} + 1) + f^{\text{nano}} (\cos \theta_Y^{\text{nano}} + 1) - 1 \quad (4)$$

where  $f^{\text{micro}}$  and  $\theta_Y^{\text{micro}}$  ( $f^{\text{nano}}$  and  $\theta_Y^{\text{nano}}$ ) are the liquid–solid contact fraction of the microstructure (nanostructure) and the Young's contact angle on the microstructure (nanostructure), respectively. If the microstructure frames and the interior nanostructure both are intrinsically hydrophobic, the superhydrophobicity of the surface can still be guaranteed after abrasion damage. Actually, apart from the geometry property, the mechanical stability of microstructures depends also on the material properties, such as the strength, ductility, hardness, fatigue resistance, and so on. Therefore, the choice of materials for fabricating the microstructure armor by considering the wettability together with the general mechanical properties is of great significance.

The wettability can be manipulated by a co-action of manipulating the solid–liquid contact area and the Young's contact angle. A typical example for this design is coating. A bottom-up method for creating super-repellent coatings with cyanoacrylate and fluorosilanes is shown in ref. [160]. Due to the locally multi-re-entrant hierarchical structures and the low-surface-energy mixture of the coatings, the coated surface shows superhydrophobicity with regard to diverse liquids ( $>100$ ) including the ultralow surface tension liquids ( $<20 \text{ mN m}^{-1}$ , such as *n*-hexane and *n*-pentane). The coatings also exhibit transparent, long-lasting, mechanical robust, and anti-freezing qualities. Figure 5 shows the robustness of the coating and the potential for developing switchable and responsive surfaces by utilizing the fabric's stretchability. The fabrics are sprayed by the coating in the relaxed state, known as partial coating, which is in contrast to the full coating at the stretched state. For the partial coating, both superomniphilic (SOL) and

superomniphobic (SOP) regions are present simultaneously when stretching. Figure 5a–c depicts the SEM images of the partially coated fabrics that are stretched along different directions, as indicated by the arrows. Figure 5d illustrates that from the released state to twofold biaxial stretching state, the original partially coated superomniphobic fabric shows superomniphilicity property in the highlighted local region. The accessibility of local superomniphilic regions depends on the size of the area as well as the intrinsic wettability of the materials, as described by the Cassie–Wenzel equation. A robustness factor  $A^*$  has been introduced to characterize the accessibility of local regions of superomniphilicity. High values of  $A^*$  indicate a robust coating with SOP property, whereas low values of  $A^*$  means that SOL state is easily accessible. Figure 5e illustrates the wetting transitions of pentane and water for partially spray-coated fabrics under different biaxial elongation. The fabric shows good water resistance until 90% elongation while the wetting transition happens at 20% elongation for pentane. This result reveals that the substrate is hard to completely repel low surface tension liquids. The introduction of some nanoscale roughness, like the hair-like structure of lotus leaf, on the fabric can be an option, which may lead to a higher cost for manufacturing. Nevertheless, the wetting transition of the fabrics is reversible due to the stretchability, as shown in Figure 5f. After 1000 cycles of stretch–release tests, the relaxed fabrics still remain super-repellent, showing excellent mechanical durability of the coating. Compared with partially coated fabrics, the fully coated fabrics display better pentane drop repellence. For the impacting pentane drop with large Weber number ( $We = 120$ ), pentane droplets bounce off the substrate and break into satellite droplets, but still without wetting the material, as demonstrated in Figure 5g. This special coating strategy combines the multi-re-entrant nature of the texture and the low surface energy of the material, which follows the design criterion for the Cassie–Wenzel theory, namely, decreasing liquid–solid contact area fraction  $f$  and increasing the intrinsic Young's contact angle of the materials via changing the surface chemistry.

#### 4. Intermediate Wetting States

The Cassie model portrays the non-wetted condition on rough surfaces, while the Wenzel model depicts the fully wet state. These two models correspond to two extreme situations. Between these two states, there are numerous intermediate wetting states on real surfaces. A recent theoretical model in combination with experiments has been narrated in ref. [63] to address the intermediate wetting states. In this work, a mechanically patterned Si substrate is fabricated in experiments, as shown in Figure 6a,b. The micropillar has the geometrical parameters of height  $h$ , spacing between pores  $b$ , size of the square orifices of the pores  $a$ , and sidewall angle  $\alpha$ . Defining  $s = a + b$ , the solid fraction  $\Phi$  and roughness  $r_w$  are expressed as  $\Phi = (s^2 - a^2)/s^2$  and  $r_w = (s^2 - a^2 + a^2/\cos\alpha)/s^2$ , respectively. Substituting  $\Phi$  and  $r_w$  into the Wenzel and Cassie (or Cassie–Baxter) equations, we obtain

$$\text{Wenzel model: } \cos \theta^* = r_w \cos \theta_Y = \frac{s^2 - a^2 + a^2/\cos \alpha}{s^2} \cos \theta_Y \quad (5)$$

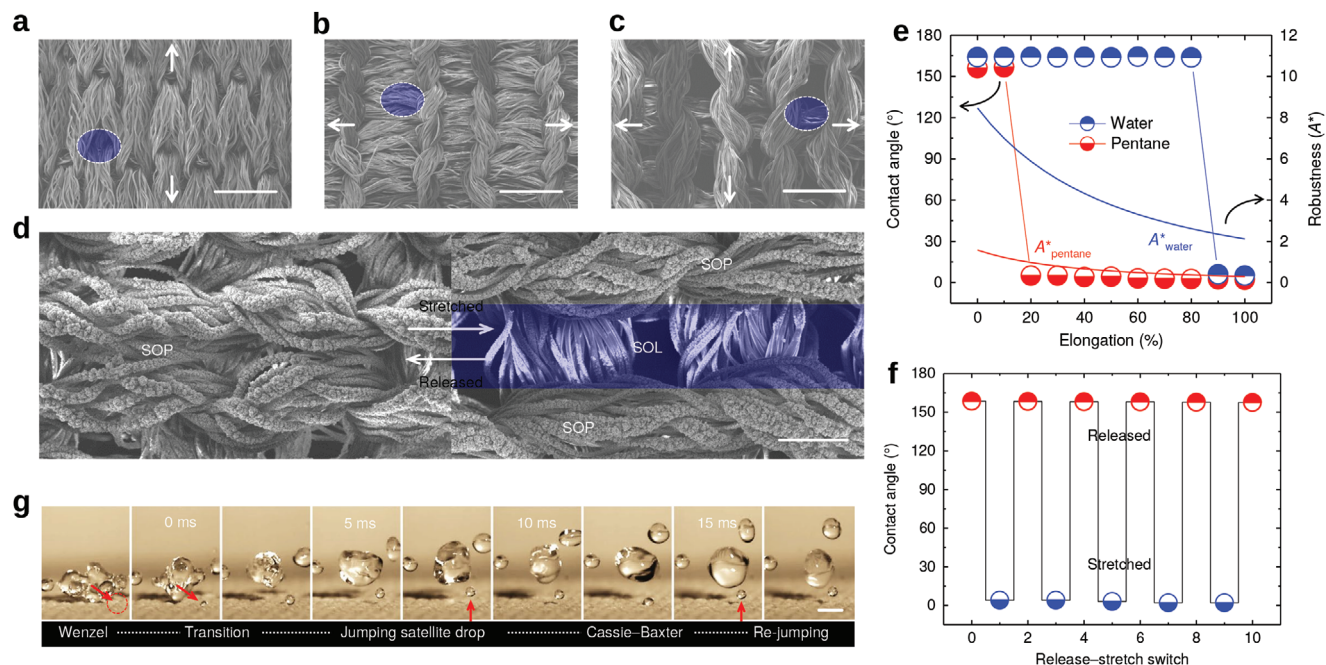


**Figure 5.** Design of coating based on the Cassie–Wenzel theory. a–c) SEM images showing partially coated polyester fabrics that are uniaxially stretched along, perpendicular to the yarn, or biaxially stretched, respectively. The polyester fabrics are coated with cyanoacrylate and fluorosilanes at the released state, which is called partially coated state. At the stretched state after coating, the fabrics have un-coated areas between the fabrics which are hydrophilic and coated area which are hydrophobic. Scale bars: 500  $\mu\text{m}$ . d) Partially coated fabric that displays superomniphobicity at the released state and superomniphobicity subject to twofold biaxial stretching. Scale bar: 200  $\mu\text{m}$ . e) Dependence of apparent contact angle and robustness factor  $A^*$  on biaxial elongation of the fabric. f) Restorability of *n*-pentane apparent contact angles during release–stretch testing cycles. g) Extruded jumping satellite droplet after an impinging *n*-pentane droplet bounces off the fully PTFE/BCA-coated fabric. Scale bar: 1 cm. a–g) Reproduced with permission.<sup>[160]</sup> Copyright 2018, Springer Nature.

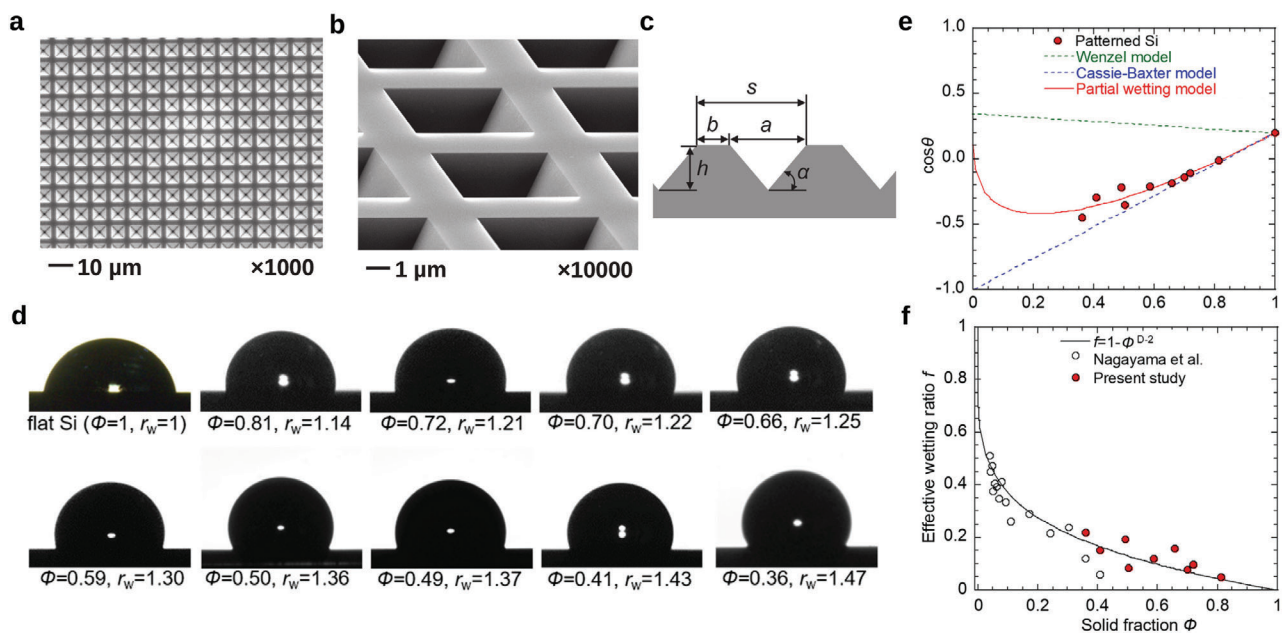


**Figure 6.** Intermediate wetting states. a) Top view and b) inclined view of a mechanically patterned Si surface. c) Sketch for the geometry of the surface heterogeneity with parameters of pore distance  $a$ , pore size  $b$ , height  $h$ , and sidewall angle  $\alpha$ . d) Wetting morphologies on the mechanically patterned Si surface with different solid area fraction  $\Phi$  and roughness  $r_w$ . e) Comparison of experimental results and theoretical models for the wetting angle on the patterned Si surface. Red circle: experimental results; blue line: Cassie–Baxter model; green line: Wenzel model; red line: partial wetting model. f) Effective wetting ratio  $f$  of solid–liquid contact area inside the pore as a function of the solid fraction  $\Phi$  from experiments and an empirical equation  $f = 1 - \Phi^{D-2}$ , where  $D$  is the fractal dimension. a–f) Reproduced with permission.<sup>[63]</sup> Copyright 2021, Elsevier.

$$\begin{aligned} \text{Cassie–Baxter model: } \cos \theta^* &= \Phi \cos \theta_Y + (1 - \Phi) \cos 180^\circ \\ &= \frac{s^2 - a^2}{s^2} \cos \theta_Y - (1 - \Phi) \end{aligned} \quad (6)$$

As depicted in Figure 6d for  $\Phi = 1$ , the Young's contact angle on a flat Si substrate is about  $78.6 \pm 1^\circ$ . By varying the geometrical parameters to decrease the solid fraction  $\Phi$  and the roughness  $r_w$ , the apparent contact angle gradually increases (Figure 6d). The experimentally measured apparent contact angle  $\theta^*$  as a function of the solid fraction  $\Phi$  is compared with the Wenzel and Cassie equations, as shown in Figure 6e. When the solid fraction is unity, the experimental results, Wenzel angle, and Cassie angle all are the same. With a decrease in  $\Phi$ , the experimental results deviate from both Wenzel and Cassie theories, but are more close to a modified Cassie–Wenzel equation

$$\begin{aligned} \text{Partial wetting model: } \cos \theta^* &= [\Phi + (r_w - \Phi)f] \cos \theta_Y \\ &+ (1 - \Phi)(1 - f) \cos 180^\circ \end{aligned} \quad (7)$$

This equation describes the intermediate wetting state where the liquid partially penetrates into the pore (Figure 2h). The mathematical derivation for this equation is shown in ref. [112]. In this derivation, an effective wetting ratio  $f$  has been introduced to calculate the solid–liquid and the liquid–gas contact areas. The effective wetting ratio  $f$  is defined as the solid–liquid contact area to the apparent contact area inside the pore, ranging between 0 (Cassie) and 1 (Wenzel). A value of  $f$  between 0 and 1 indicates a partial wetting state. By using the parameter  $f$ , the real contact area ratios of solid–liquid  $\Phi_{sl}$ , and liquid–gas  $\Phi_{lv}$  to the flat substrate are expressed as  $\Phi_{sl} = \Phi + (r_w - \Phi)f$  and  $\Phi_{lv} = (1 - \Phi)(1 - f)$ , respectively. With these two parameters, we obtain the partial wetting model via replacing  $\Phi$  by  $\Phi_{sl}$  and  $1 - \Phi$  by  $\Phi_{lv}$  in the Cassie–Baxter equation. The partial wetting model shows better agreement with experimental data than the Wenzel and Cassie–Baxter models, providing a strong evidence for the existence of the intermediate wetting states. The effective wetting ratio  $f$  can be estimated according to Equation (7) with the experimental value for the apparent contact angle  $\theta^*$ , the Young's contact angle  $\theta_Y$ , the geometrical parameters  $\Phi$ , and the roughness factor  $r_w$  as  $f = [\cos \theta^* - \Phi \cos \theta_Y + (1 - \Phi)] / [(r_w - \Phi) \cos \theta_Y + (1 - \Phi)]$ . The estimated value of  $f$  as a function of the solid fraction  $\Phi$  has been shown to be consistent with an empirical relation  $f = 1 - \Phi^{D-2}$  (Figure 6f). Here,  $D$  denotes the fractal dimension.

The proposed theoretical model provides a clue to quantitatively explore the diverse wetting states on real roughness surfaces. However, it relies on the precise measurements of the solid fraction and the effective wetting area at hydrophobic solid–liquid interface, which is very challenging when the structure has a complex geometry with multiscale and hierarchical structures. Besides, the model has shown its consistency for wetting on structured surfaces with pores mainly in micrometer scale but the validity for pores with other length scales still needs further verification and investigation. By considering the nano/micro hierarchically structured surface and assuming the similar wetting behavior at nano/micro length scales, a partial wetting model has been derived in ref. [112].

From Young, Cassie–Baxter, and Wenzel equations, the apparent contact angle depends only on the intensive variables. In the

Cassie–Baxter model, the apparent contact angle depends on the porosity  $\Phi$ . When the droplet is much larger than roughness, the value of  $\Phi$  is intensive. However, when the droplet size is compared with the surface heterogeneity,  $\Phi$  varies with the droplet volume. Moreover, by taking the curved liquid–air interface in the air pocket into account, the parameter of effective wetting ratio  $f$  affects the apparent contact angle  $\theta^*$ , as demonstrated by energy minimization method in the partial wetting model. It comes to a question if the effective wetting ratio  $f$  is affected by the droplet volume or not. In ref. [63], the droplet volume is fixed and the effect of the droplet volume on the effective wetting ratio  $f$  needs more investigations to conclude if  $\theta^*$  only depends on intensive variables in the partial wetting model.

## 5. Anisotropic Wetting Morphologies

In the Cassie–Wenzel theory, the droplet is in the shape of a spherical cap. The triple line where the droplet, the surrounding phase, and the substrate meet can be interpreted by a kind of statistical average along the circumference in accordance with the probability of the area fraction  $f_i$ . This is justified when the droplet diameter is much larger than the characteristic length of the heterogeneity. In this case, the occurrence of the  $i$ -heterogeneity at the triple line region is somehow consistent with the individual area fraction  $f_i$ . Noteworthy, it should not be misinterpreted that the wetting effect on patterned substrates is solely determined by the physics alone in region of the triple line. Rather, the wetting effect is a result of the global energy minimization. When the droplet size is comparable with the characteristic length of the heterogeneity, the global energy minimization often leads to anisotropic wetting morphologies. Due to the occurrence of metastable/intermediate states as well as intricate energy barriers between the metastable states, it is challenging to reproduce previous results, leading to the difficulty for materials design. However, one can deliberately design particular substrates with characteristic length comparing with the size of the droplet. In this way, the anisotropic wetting morphologies are controllable. In this section, we will overview the formation of anisotropic wetting morphologies affected by droplet volume, deposition position of the droplet, the shape, the orientation, and the arrangement of the surface heterogeneity. We will start with the stripped patterned substrate, which is a kind of 1D heterogeneity, where the energy minimal states are predictable. Thereafter, we will overview some progresses for addressing the anisotropic wetting behavior on substrates with 2D heterogeneity. At last of this section, we will highlight the wetting behavior on a substrate with 3D heterogeneity, which is the so-called capillary ratchet.

### 5.1. Effect of Droplet Volume, Spreading, and Contact Angle Hysteresis

Figure 7I shows the spreading of a 3  $\mu$ L water droplet over a chemically patterned substrate from experiments (top panel), lattice-Boltzmann simulation (middle panel), and phase-field simulation (bottom panel). The surface is made of self-assembled SiO<sub>2</sub> and PFDTs stripes, which are hydrophilic and hydrophobic with Young's contact angle of 40° and 110°, respectively. The widths

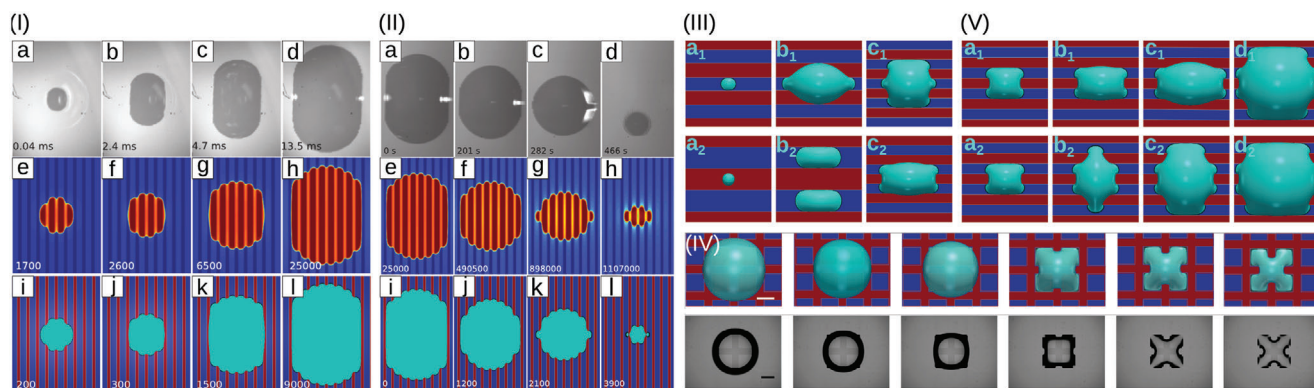


**Figure 7.** Effect of droplet volume and spreading on the formation of anisotropic wetting morphologies and contact angle hysteresis on chemically patterned substrate. I) Spreading of a 3  $\mu\text{L}$  water droplet on a chemically stripped patterned substrate consisting of a silicon dioxide ( $\text{SiO}_2$ ) stripe and a perfluorodecyltrichlorosilane (PFDT) stripe. The widths of the  $\text{SiO}_2$  and PFDT stripes are 20 and 10  $\mu\text{m}$ , respectively. The apparent contact angles of water on the  $\text{SiO}_2$  and PFDT stripes are  $40^\circ$  and  $110^\circ$ , respectively. Experiments: (a–d). Lattice Boltzmann simulation: (e–h). I–a–h) Reproduced with permission.<sup>[161]</sup> Copyright 2013, American Physical Society. Phase-field simulations (i–l). I–i–l) Reproduced with permission.<sup>[79]</sup> Copyright 2019, American Chemical Society. II) Evaporation of a 1  $\mu\text{L}$  water droplet on the same substrate shown in (I). Experiments: (a–d). Lattice Boltzmann simulation: (e–h). II–a–h) Reproduced with permission.<sup>[161]</sup> Copyright 2013, American Physical Society. II–i–l) Phase-field simulations. Reproduced with permission.<sup>[79]</sup> Copyright 2019, American Chemical Society. III) The equilibrium wetting morphologies on a stripped patterned substrate with a uniform width of  $d$  for different droplet volumes  $V$ :  $d/V^{1/3} = 2.5$  ( $a_1, a_2$ );  $d/V^{1/3} = 1.1$  ( $b_1, b_2$ );  $d/V^{1/3} = 0.35$  ( $c_1, c_2$ ). The local Young's contact angles on the red and blue stripes are  $106^\circ$  and  $41^\circ$ , respectively. The droplet center is placed on the blue stripe in ( $a_1$ – $c_1$ ) and on the red stripe in ( $a_2$ – $c_2$ ). III) Reproduced with permission.<sup>[79]</sup> Copyright 2019, American Chemical Society. IV) The evaporation process of a 20  $\mu\text{L}$  water droplet on a lattice patterned substrate from simulations and experiments. Apparent contact angles for the water droplet on hydrophilic (blue) and hydrophobic (red) areas are  $0^\circ$  and  $160 \pm 10^\circ$ , respectively. The substrate is made of glass. The chemical pattern is achieved by a two step UV-light-driven thiol–ene modification through the photomask. The center-to-center distance of two neighboring hydrophilic spots is 0.5 mm. IV) Reproduced with permission.<sup>[82]</sup> Copyright 2022, Elsevier. V) Quasi-equilibrium condensation ( $a_1$ – $d_1$ ) and evaporation ( $a_2$ – $d_2$ ) of a water droplet on the chemically patterned substrate depicted in (III). The ratio of the stripe width to the droplet size is  $d/V^{1/3} = 0.5$  ( $a_1, a_2$ );  $d/V^{1/3} = 0.4$  ( $b_1, b_2$ );  $d/V^{1/3} = 0.3$  ( $c_1, c_2$ );  $d/V^{1/3} = 0.23$  ( $d_1, d_2$ ). V) Reproduced with permission.<sup>[79]</sup> Copyright 2019, American Chemical Society.

of the  $\text{SiO}_2$  and PFDT stripes are 20 and 10  $\mu\text{m}$ , respectively. With time, the droplet spreads faster in the parallel direction ( $y$ -dimension) than in the direction perpendicular to the stripe ( $x$ -dimension), leading to an anisotropic wetting morphology with a pronounced elongation along the stripe. Anisotropic wetting morphologies are also observed in the evaporation process of a 1  $\mu\text{L}$  water droplet, as illustrated in Figure 7II. The substrate for the evaporation experiments is the same as the one for the spreading in Figure 7I. In the evaporation process, the droplet reduces its volume with time and tends to have a circular base area contrary to the strong anisotropic morphology at the initial stage.

The anisotropic wetting morphologies shown in Figure 7I,II can be interpreted by the contact line pinning–depinning mechanism. In the  $x$ -dimension, the pinning force due to the variation of the wall free energy occurs at the boundary of the  $\text{SiO}_2$ –PFDT stripe, constraining the free movement of the contact line. In the  $y$ -dimension, the droplet freely moves inward in the evaporation case and outward in the spreading case; the position of the contact line is determined by the Young's contact angles on the hydrophilic and hydrophobic stripes subjected to the geometrical constraint of volume. The free movement of the droplet in  $y$ -dimension leads to a non-spherical cap. To reduce the total energy of the system, the droplet has to move in the  $x$ -direction, giving rise to the depinning effect at the boundary of the  $\text{SiO}_2$ –PFDT stripe. Physically, the pinning–depinning mechanism is caused either by the geometry of the heterogeneity which affects the local normal vector or by the wall energy variation (see Section 6 for more details). In the pinning–depinning process, the so-called “stick–slip–jump” behavior is often observed. In the stick

stage, the droplet freely moves in the  $y$ -direction but is pinned at the boundary of the  $\text{SiO}_2$ –PFDT stripe, leading to an aspect ratio greater than unity. In the slip stage, the contact line slips over the hydrophilic strip toward the next adjacent hydrophilic–hydrophobic boundary. In the third stage, the contact line is again pinned at the boundary and jumps to next hydrophilic strip due to the depinning effect. The “stick–slip–jump” behavior has been studied by many other scientists.<sup>[162]</sup>

Figure 7III,V illustrates the effect of volume and kinetics on the metastable states, respectively, from the phase-field simulations. The Young's contact angle on the red and blue stripes is  $106^\circ$  and  $41^\circ$ , respectively. The red and blue stripe has the same width  $d$ . The droplet size with respect to the stripe width is depicted by  $d/V^{1/3}$ , where  $V$  is the volume of the droplet. As shown in Figure 7III( $a_1$ ), a relatively small droplet deposited on the blue stripe stays only on the hydrophilic stripe, where the droplet has a spherical cap; the apparent contact angle is fully described by the Young's law. With a further increase in the volume, the droplet exhibits the stick–slip–jump behavior and occupies more stripes. However, when a droplet is deposited on a different position, the hydrophobic stripe (Figure 7III( $a_2$ – $c_2$ )), the effect of volume on the wetting morphology differs from the one shown in Figure 7III( $a_1$ – $c_1$ ). For an intermediate volume, the droplet breaks up into two independent droplets (Figure 7III( $b_2$ )). This breakup is due to the interfacial instability, which is out of the scope of the present overview. We refer to refs. [71, 163, 164] for a systematic study of the droplet breakup.

Figure 7II,III both demonstrate that different droplet volumes have distinct energy minima states on a stripped patterned

substrate. For a more complex patterned substrate, the energy minima state and the corresponding wetting morphologies become more hard to be elucidated. Figure 7IV shows the equilibrium wetting morphologies on a lattice patterned substrate for the evaporation of a water droplet starting with a volume of 20  $\mu\text{L}$ . The experimentally observed anisotropic wetting shapes at each time are well consistent with the simulation results. Noteworthy, for a fixed droplet volume, the equilibrium morphologies are not unique on the same substrate even when the droplet is on the same position. The different metastable state for a constant volume on the same position is known as the so-called contact angle hysteresis. It has been well studied in literature that surface roughness leads to the advancing and receding contact angles. We refer to refs. [165, 166] for surface roughness induced contact angle hysteresis. Figure 7V shows the phenomenon of contact angle hysteresis on a chemically patterned substrate by considering the condensation and evaporation processes. From ( $a_1$ ) to ( $d_1$ ), the droplet volume increases (condensation); from ( $d_2$ ) to ( $a_2$ ), the droplet volume decreases (evaporation); In ( $a_1$ ) and ( $a_2$ ), ( $b_1$ ) and ( $b_2$ ), ( $c_1$ ) and ( $c_2$ ), and ( $d_1$ ) and ( $d_2$ ), the droplet has the same volume. However, the equilibrium wetting pattern in ( $b_1$ ) is distinct from that in ( $b_2$ ) though the droplet has the same volume and is on the same position. The difference is also observed in ( $c_1$ ) and ( $c_2$ ). The contact angle hysteresis is often explained by the contact line pinning. In the condensation process, the contact line is pinned at the hydrophilic and hydrophobic boundary of the droplet side. Whereas the contact line is stucked at the hydrophilic and hydrophobic boundary of the surrounding side in the evaporation process, leading to distinct energy minimization path. The results show that for the volume in ( $b_1$ ) and ( $b_2$ ), the system has at least two metastable states. The selection of which metastable state for the droplet depends on the energy map and the energy minimization path, which are elucidated in the next section.

## 5.2. Effect of Deposition Position

On the 1D stripped patterned substrate, the metastable states of the droplet can be more or less feasibly comprehended, when the droplet volume is relatively small. With an increase in the droplet volume, the number of the metastable states increases divergently, which makes it hard for materials design and for reproduction of previous results. When considering a 2D or higher dimensional substrate, like the lattice pattern, chessboard pattern, the situation becomes more complicated. A generalized theoretical model in combination with numerical simulations and experiments has been proposed in refs. [81, 82] to address the metastable states for symmetrical wetting morphologies. In the theoretical method, the base area of the droplet is assumed to be depicted by an ellipse with major and minor axes of  $a$  and  $b$ , which are variables corresponding to different droplet states. The droplet volume depends these two variables as well as the height  $h$  of the droplet,  $V = V(a, b, h)$ . Subject to the constraint of a constant volume, the total interfacial energy  $S$  is calculated as a function of  $a$  and  $b$ , namely  $S(a, b)$ . Here,  $S$  has contribution from the liquid–gas cap, which is assumed to be spherical, and the deduction from the base contact area with the defined functions for the surface heterogeneity. The particular functions for

stripped patterned, lattice patterned, and chessboard patterned substrates are given in ref. [81]. Each local minimum value in the energy landscape according to  $S(a, b)$  predicts a metastable state. In between these metastable states, there are energy barriers. With this prediction for the metastable state, the base area of the droplet at equilibrium has an aspect ratio of  $a/b$ . This energy map method has been applied to stripped patterned, lattice patterned, and chessboard patterned substrates, which have been confirmed by simulation and experiments.

Some selective results for the energy map method are presented in Figure 8. Figure 8I shows the energy landscape  $S(a, b)$  when the droplet is deposited on different positions on a lattice patterned substrate. The ratio of the droplet radius to the lattice size is 0.75. The Young's contact angle on the red lattice and the blue matrix are  $120^\circ$  and  $60^\circ$ , respectively. When the droplet is placed at the center of four neighboring lattice, the energy landscape has one minimum, as highlight by the number "1" in Figure 8I(a). At this local minimum state, the major and minor radii  $a$  and  $b$  are the same, indicating a nearly circular base area. The confirmation of this minimum state via phase-field simulation is shown in the bottom panel of Figure 8I(a). When the droplet is deposited at the center of two adjacent lattices and exactly on the red lattice, we observe one minimum ("2") and three minima ("3", "4", "5"), respectively. At the minimum "2," the radius  $b$  is larger than  $a$ , indicating an elongated state. At the minimum "3" and "5," the radius  $b$  is greater and smaller than  $a$ , respectively, revealing an elongated wetting morphology in different directions. The minimum state "4" has the same value of  $a$  and  $b$ , representing a circular base area. All of these minimum states are corroborated well by the numerical simulations; the dashed red line depicts the base line according to the value of  $a$  and  $b$  in the energy map. Note there are energy barriers between the three minima states in Figure 8I(c). In this case, the final shape of the droplet depends on the initial aspect ratio, which has been used to guide the simulation for setting up the droplet shape at the beginning. By using the energy map method to guide the simulation, 14 metastable states have been addressed on a chessboard patterned substrate, as demonstrated in Figure 8II.

The energy map method has been compared with experiments on the lattice patterned substrates, as shown in Figure 8III,IV. Here, two different lattice shapes, square and circle, are considered. The position of the lattice beneath the droplet from simulation and experiments is highlighted by the black dashed curves. Good agreement between the energy map method, numerical simulation, and experiments are observed. In spite of these good agreements, the energy map method is not a "panacea." The advantage of the energy map method is its explanation of the numerous rotationally symmetric wetting morphologies. The energy map method can provide some guidelines for the experiment to achieve the demanded anisotropic wetting shapes by manipulating the initial aspect ratio of the liquid, the deposition position, the droplet volume without blind tries. It can also explain which anisotropic wetting morphology is more easily obtained by justifying which metastable state has a relatively low energy. However, some metastable states are missed in the energy map method, such as the axially symmetric shape (last subfigure in Figure 8IV and in Figure 8III(a)) and the state of droplet breakup. The reason behind is that the assumption of the elliptic base area cannot be applied for the axially symmetric base area,

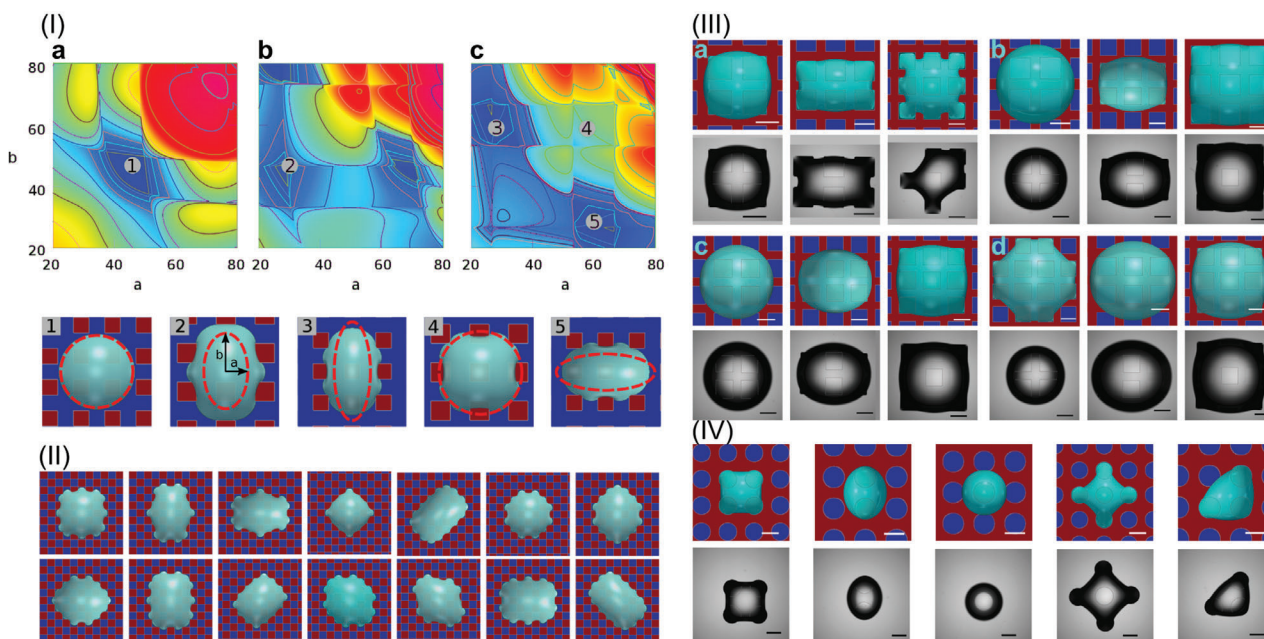


**Figure 8.** Energy map method for metastable states and the effect of the droplet position on the anisotropic wetting morphologies. I) Top: Contour plot for the interfacial energy of the system  $S(a,b)$  on a lattice patterned substrate when the droplet is deposited at the center of four neighboring lattices (left), at the center of two adjacent lattices (middle), and exactly on the lattice (right). The ratio of the lattice size to the radius of the droplet is 0.75. The Young's contact angles on the hydrophobic (red lattice) and the hydrophilic (blue matrix) area are  $120^\circ$  and  $60^\circ$ , respectively. Bottom: The wetting morphologies from the numerical simulation and the energy map method. The labels "1," "2," "3," "4," and "5" correspond to the energy minimum highlighted in the top panel of the energy landscape. The elliptic dashed line is obtained according to the value of  $a$  and  $b$  at the minimum state in the energy landscape. II) Fourteen metastable states predicted from the energy map method and the numerical simulations on a chessboard patterned substrate. The Young's contact angle on the red and blue areas is  $90^\circ$  and  $30^\circ$ , respectively. The ratio of the lattice size to the radius of the droplet is 1. I, II) Reproduced under the terms of the CC-BY Creative Commons Attribution 3.0 Unported license (<https://creativecommons.org/licenses/by/3.0/>).<sup>[81]</sup> Copyright 2020, Royal Society of Chemistry. III, IV) Wetting morphologies on a chemically patterned substrate with square and circular lattices, respectively. The droplet volumes in (III(a-d)) and (IV) are 10, 25, 30, 40, and  $5\mu\text{L}$ , respectively. The side length of the square lattice and the diameter of the circular lattice both are 1 mm. The Young's contact angle of water on the lattice and matrix are  $0^\circ$  and  $160 \pm 10^\circ$ , respectively. Scale bar: 1 mm. In each subfigure, the position of the droplet is different. The position of the lattice beneath the droplet is highlighted by the present authors with the dashed lines. III, IV) Reproduced with permission.<sup>[82]</sup> Copyright 2022, Elsevier.

which largely deviates from an ellipse. A perspective is a more accurate description of the base line. Another shortcoming of the energy map method is the assumption of the quasi-equilibrium, which overlooks the kinetic energy. The kinetic energy can surmount the energy barrier to reach a distinct adjacent metastable state in the energy map. The transformation of the kinetic energy and the free energy can be intrinsically induced by the Kortweg stress, which is out of the scope of this review. For more discussions, we refer to refs. [167, 168].

### 5.3. Manipulation of Droplet Shapes by Man-Made Substrates

Given the complexity of the metastable states due to surface heterogeneity, one can design the surface by assigning the position, the shape, and the arrangement of the heterogeneity to achieve controllable wetting morphologies. When the man-made heterogeneity is much larger than the intrinsic roughness, the energy barriers in the Cassie–Wenzel theory resulting from the surface roughness tend to be irrelevant. Particular wetting morphologies can be obtained by designing the surface heterogeneity. **Figure 9I** shows the formation of line, quadrilateral, star, hexagonal, octagon wetting patterns on man-made patterned substrate

via inkjet printing.<sup>[169]</sup> The heterogeneous substrate is obtained through photolithography and then postgrafted with perfluorooctanesulfonic acid (PFOS). After removing the photoresist, the preprotected region shows hydrophilicity which acts as the hydrophilic pinning pattern, while the unprotected region is hydrophobic. The hydrophilic point has a circular shape with a diameter of  $\approx 10\mu\text{m}$ . By setting the location of the hydrophilic points, desired anisotropic wetting morphologies are obtained when printing ink solution on the substrate. The stability of the meniscus formed between the hydrophilic spots has also been studied in this work. With an increase in the solute concentration in the ink, the surface tension increases, which leads to a breakup of the meniscus. These controllable 3D printing structures have been used for information carriers.<sup>[169]</sup>

A more complex heterogeneous substrate has been designed in ref. [106] to achieve polygonal non-wetting droplets. The mechanically patterned surface consists of silicon hydrophobic pillars in the shape of triangle, circle, and square. The Young's contact angle on the smooth substrate is  $110 \pm 5^\circ$ . The cross section of the micropillars is shown by the white area in Figure 9II(b–d). In the wetting experiments, a superhydrophilic plate is placed on top to press the droplet that is deposited on the patterned substrate. By manipulating the arrangement of the

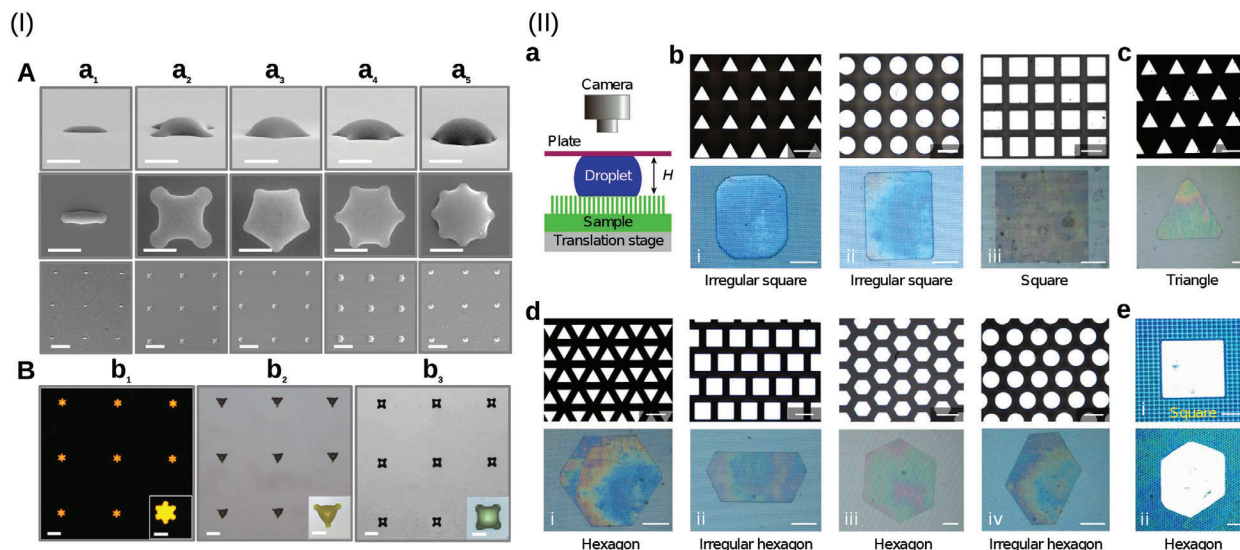


**Figure 9.** Man-made patterned substrate for designing anisotropic wetting morphologies. I) Manipulation of anisotropic wetting morphologies through assigning the position of the hydrophilic chemical pattern. A) 3D inkjet printing structures include line ( $a_1$ ), quadrilateral ( $a_2$ ), star ( $a_3$ ), hexagonal ( $a_4$ ), and octagon ( $a_5$ ). The top, middle, and bottom panels are side-view, top-view, and arrayed SEM images of the corresponding morphologies, respectively. Scale bar: 20  $\mu\text{m}$  for the top and middle panels, and 100  $\mu\text{m}$  for the bottom panel. B) The wetting morphologies of ink solution composed of various materials: CdTe quantum dots ( $b_1$ ), silver nanoparticles ( $b_2$ ), and manganese chloride salt ( $b_3$ ). Insets are enlarged images of a printing unit. Scale bar: 50  $\mu\text{m}$  for the printing pattern and 20  $\mu\text{m}$  for the inset. I) Reproduced with permission.<sup>[169]</sup> Copyright 2015, Wiley-VCH. II) Anisotropic wetting morphology via changing the arrangement of the micropillars on mechanically patterned substrate. a) Sketch for the experimental setup, where the droplet is confined between the patterned substrate and a superhydrophilic glass plate. b) Square arrangement of the triangular, circular, and square micropillar (top) and the corresponding wetting patterns for water droplets (bottom). c) Triangular water droplet pattern created by a triangular arrangement of microtextures with a triangular cross-section. d) Hexagonal and irregular hexagonal water droplet patterns created by the hexagonal arrangement of microtextures with triangular, square, hexagonal, and circular cross-sections. e) Square and hexagonal liquid metal (Galinstan) droplet patterns. (e-i) and (e-ii) have the same geometrical topologies (cross-section of micropillar and arrangement of array) as (b-ii) and (d-i), respectively. Scale bars for the micropillar arrays: 20  $\mu\text{m}$ . Scale bars for the droplet patterns: 500  $\mu\text{m}$  for (b–d), and 200  $\mu\text{m}$  for (e). II) Reproduced under the terms of the CC-BY Creative Commons Attribution 4.0 International license (<https://creativecommons.org/licenses/by/4.0>).<sup>[106]</sup> Copyright 2022, The Authors, published by Springer Nature.

micropillars to be square, triangle, and hexagonal, the confined droplet takes the square, triangle, and hexagonal shapes, respectively. In comparison with the arrangement of the pillars, the shape of the pillar itself is found to be of secondary importance affecting the wetting morphologies. In this study, the droplet is extruded by the top glass plate, so that the Wenzel state is reached. By this way, the wetting morphology is largely affected by the arrangement of the surface heterogeneity, for example, a hexagonal arrangement leading to a hexagonal wetting morphology. This observation is consistent with the simple experiments shown in Figure 9I that two hydrophilic spots lead to a line wetting and that three hydrophilic spots result in a triangle wetting, etc. When removing the superhydrophilic plate on the top, the droplet is released and always takes the spherical shape, which corresponds to the Cassie state. A similar surface design via square, rectangular, hexagonal arrangement of chemical heterogeneity on the surface has been provided in ref. [105]. The key point of these designs is how to achieve the Wenzel state which is mainly affected by the location of the heterogeneity.

#### 5.4. Effect of 3D Curvature

The stripped patterned substrate, either chemical or mechanical, belongs to the sort of 2D heterogeneity. For the mechanically patterned substrate, the mean curvature in the dimension parallel

to the substrate is zero; the curvature has only contribution from the direction perpendicular to the stripe. The chessboard and lattice patterned substrates are in the class of 3D heterogeneity. In the mechanically patterned substrate considered in the Cassie–Wenzel theory (Figure 2), the mean curvature has the radial curvature affected by the diameter of the pillar and the edge curvature at corners of the pillar. The micropillar is perpendicular to the substrate. By changing the orientation angle of the micropillar, one can achieve directional movement of the droplet. One typical example of this application for materials design is capillary ratchet.

As shown in Figure 10I(c,d), two liquids, ethanol and water are placed on the araucaria leaf. The ethanol spreads spontaneously along the tiling direction of the leaf (defining as forward direction), while the water transports in the opposite direction. Based on this observation, araucaria leaf inspired surface has been designed in ref. [97]. The designed surface has several parallel ratchet arrays with pitch  $p$ , tilting angle  $\alpha$ , vertical height  $h$ , row-to-row width  $w$ , inside-to-inside length  $d$ , and bottom-to-top length  $l$  (Figure 10I(b)). Note that the ratchet has a transverse curvature  $R_1$  and a longitudinal curvature  $R_2$ , as depicted in Figure 10II(a,b). By mixing the water with ethanol, the liquid mixture spreads forward when the mixture has more ethanol and backward when the mixture contains more water. A bidirectional spreading is obtained for liquid mixture with an intermediate concentration. This directional movement is in

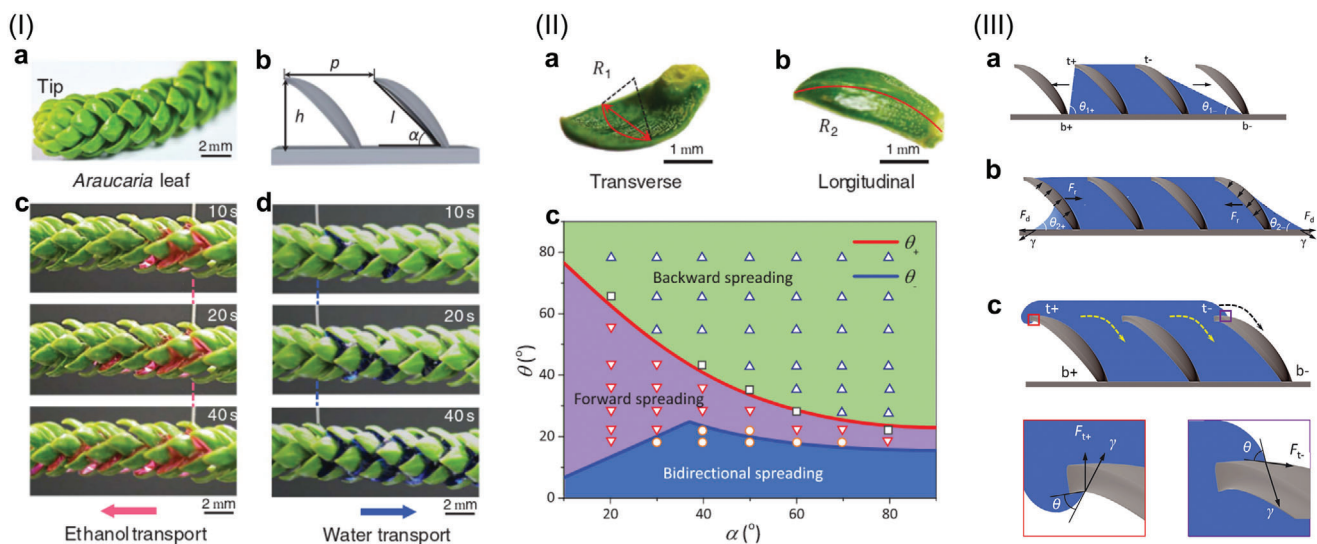


**Figure 10.** 3D capillary ratchet. I) Araucaria leaf and directional movement of liquid. a) Optical image of an araucaria leaf. b) Structural characteristics of an araucaria leaf with height ( $h$ ), tip-to-tip pitch ( $p$ ), length ( $l$ ), and tilt angle  $\alpha$ . c) Ethanol spreads along the ratchet-tilting direction (forward direction). d) Water moves in the opposite direction (backward direction). II) a, b) Illustration of the transverse (a) and longitudinal (b) curvature of an araucaria leaf. c) Phase map for the directional steering of liquid transport. When  $\theta_- < \theta < \theta_+$ , liquid spreads forward. When  $\theta > \theta_+$ , liquid spreads backward. When  $\theta$  is  $\theta_+$  (symbols marked with rectangle) or  $\theta < \theta_-$ , the liquid manifests a bidirectional transport. III) Sketch for the mechanism of the direction movement on the bottom plane (a, b) and on the tip (c). I–III) Reproduced with permission.<sup>[97]</sup> Copyright 2022, AAAS.

contrast to the 1D or 2D structures, where the liquids of water and ethanol exhibit only bidirectional motion. The mechanism for the directional movement is sketched in Figure 10III(a–c), which show the effect of the two curvature radii,  $R_1$  and  $R_2$ . The critical state for the forward and backward movement is determined by two factors at the very left ratchet shown in Figure 10III(a). One is the geometrical constraint; the other factor is the force balance on the bottom plane of the ratchet structure at the  $b_+$  side. The geometrical constraint gives rise to a critical angle  $\theta_{1+} = \arctan[l \sin \alpha / (p - l \cos \alpha)]$ . A forward movement is possible only when the Young's contact angle is less than  $\theta_{1+}$ , which means that the chemistry hydrophilicity is more pronounced than the structure hydrophilicity. When  $\theta > \theta_{1+}$ , backward spreading is possible. The force balance at  $b_+$  consists of the forward capillary force  $F_d$  and the backward resistance force  $F_r$ , leading to another critical angle  $\theta_{2+}$  for the forward and backward movement at  $b_+$ . The forward capillary force is scaled by the distance of the ratchet as  $d\sigma \cos\theta$  and the backward resistance force is expressed as  $2l\sigma \sin\alpha \sin(\theta + \beta)$ , where  $\beta$  is the semiangle for the transverse ratchet arc. The minimum value of  $\theta_{2+}$  and  $\theta_{1+}$  differentiates the critical state for forward and backward movement, as shown by the red line in Figure 10II(c). The critical state for the forward and bi-directional spreading is depicted by the blue solid line in Figure 10II(c). This critical line is obtained by analyzing the geometrical constraint and the force balance at the  $b_-$  side, as sketched in Figure 10III(a). The value of  $\theta_{2-}$  is due to the geometrical constraint and the value of  $\theta_{2-}$  is a result of the force balance between  $F_r$  and  $F_d$ . The minimum value of  $\theta_{1-}$  and  $\theta_{2-}$  defines the solid blue line discriminating forward and bi-directional spreading. The force balance together with the geometrical constraint addresses moving direction of the liquid but cannot explain the pinning effect at the tip of the araucaria leaf. As proposed in ref. [97], the reentrant structure at the  $t_+$  side pro-

duces an upward capillary force, pinning the liquid at the tip of the leaf, whereas this pinning effect is absent at the  $t_-$  side, as illustrated in Figure 10III(c). This pinning effect is similar to the “tea-pot” phenomenon. When we continuously add water into a tea pot or a cup, the water reaches the top round edge of the container, but does not spill out because of the pinning effect at the edge of the container. Only when the volume of the liquid reaches a critical value, it overflows. The design of the 3D ratchet structure enables a promising liquid transport technique, which allows the control of the liquid transport direction based on the surface structure as well as the surface tension.

## 6. Thermodynamic Interpretation for the Wetting Effect on Patterned Substrate

There are distinct explanations and modeling approaches for the anisotropic wetting effect on chemically and mechanically patterned substrate. The anisotropic wetting morphologies are often explained by the pinning and depinning effect near the contact line.<sup>[170]</sup> In this section, we summarize a thermodynamic interpretation to comprehend the pinning and depinning effect. Before the summation, we overview a natural boundary condition which has been used in lots of literature<sup>[79,167]</sup> for simulating the wetting mechanism.

According to van der Waals, Cahn,<sup>[171]</sup> and Landau,<sup>[172]</sup> the free energy density of a non-uniform system depends on the fluid density  $\rho$  and its gradient  $\nabla\rho$ , namely,  $f = f(\rho, \nabla\rho)$ . With this function, the free energy of the system can be written as  $\mathcal{F}(\rho, \nabla\rho) = \int_{\Omega} f(\rho, \nabla\rho) d\Omega + \int_S \gamma(\rho) dS$  (Figure 11a). The first term represents the free energy contribution from the droplet-surroundings interface as well as the droplet/surroundings bulk. The second term depicts the wall potential energy, which is due to the attractive/repulsive interaction between the liquid and the solid

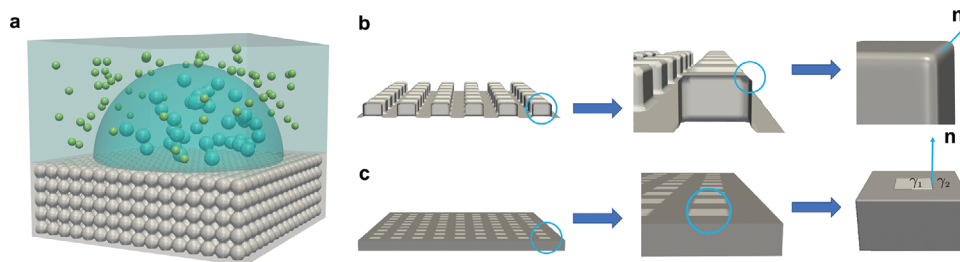


**Figure 11.** a) Schematics for the free energy contribution in the wetting system when a droplet is deposited on a homogeneous substrate. Gray: substrate atoms; cyan: droplet molecules; green: surrounding molecules (not real scaling). The interaction between the droplet molecules and the substrate atoms leads to the wall potential energy  $\gamma(\rho)$ . Apart from the potential energy at the substrate, we have the free energy density  $f(\rho, \nabla\rho)$  in the domain bulk  $\Omega$ . The free energy density  $f(\rho, \nabla\rho)$  is due to the interaction between the droplet molecules, between the surrounding molecules, and between the droplet molecule and the surrounding molecule. b) Mechanically patterned substrate: variation of the normal vector  $\mathbf{n}$  at the edge of the mechanical pillar. c) Chemically patterned substrate. The normal vector  $\mathbf{n}$  remains unchanged across the boundary of two chemical patterns, but the interface energy density varies from  $\gamma_1$  to  $\gamma_2$ .

substrate. The equilibrium state of the system is achieved by minimizing the free energy functional  $\mathcal{F}$ . At an isothermal condition, the free energy must be non-increasing with time to be consistent with the second law of thermodynamics, namely  $d\mathcal{F}/dt \leq 0$ . By using the chain rule for  $df$  with respect to  $\rho$  and  $\nabla\rho$ , one obtains the total derivative of the free energy to time as

$$\frac{d\mathcal{F}}{dt} = \int_{\Omega} \left( \frac{\partial f}{\partial \rho} - \nabla \cdot \frac{\partial f}{\partial \nabla \rho} \right) \frac{d\rho}{dt} d\Omega + \int_S \left( \frac{\partial \gamma}{\partial \rho} - \frac{\partial f}{\partial \nabla \rho} \cdot \mathbf{n} \right) \frac{d\rho}{dt} dS \leq 0 \quad (8)$$

where  $\mathbf{n}$  is the normal vector of the substrate  $S$ . On  $S$ , to reduce the free energy, the evolution of the system is chosen as

$$\frac{d\rho}{dt} = -\Gamma \left( \frac{\partial \gamma}{\partial \rho} - \frac{\partial f}{\partial \nabla \rho} \cdot \mathbf{n} \right) \quad (9)$$

where  $\Gamma$  is a positive kinetic coefficient so that the free energy is always non-increasing,  $-\int_S \Gamma (\mu_S)^2 \leq 0$ ;  $\mu_S$  is the chemical potential at the substrate defined by the expression inside the bracket of the second term in Equation (8). Most models on the wetting phenomenon in literature are based on Equation (9), such as the work of Jacqmin,<sup>[167]</sup> Cahn,<sup>[173]</sup> de Gennes,<sup>[174]</sup> and many other references.<sup>[175–179]</sup> This equation is sometimes called natural boundary condition. At static equilibrium when  $d\rho/dt = 0$ , it has been demonstrated that this boundary condition is equivalent to the Young's law.<sup>[180]</sup> Noteworthy, Equation (9) is more generalized than Young's law. The Young's law cannot be used to the case when the ratio  $(\gamma_1 - \gamma_2)/\sigma > 1$  or  $(\gamma_1 - \gamma_2)/\sigma < -1$ , which corresponds to superhydrophilic and superhydrophobic setups, respectively, while Equation (9) can be applied to any surface-tension ratios in accordance with the second law of thermodynamics.

From Equation (9), we see that the wetting effect is actually determined by two factors: i) The geometry of the surface which is characterized by the normal vector  $\mathbf{n}$ . ii) The chemical interaction between the surface and the liquid, which is characterized by the wall energy density  $\gamma(\rho)$ . The first factor is a characteristic for mechanically patterned substrates (Figure 11b). The variation of the normal vectors at the edge of the heterogeneity or

the roughness determines the forward/backward movement or stagnation of the contact line, which leads to the pinning and depinning phenomena. Note that the wetting boundary condition should be applied not only at the triple line but also at all positions on the substrate  $S$  to reduce the free energy of the system. The second factor is the chemical heterogeneity. In this case, the normal vector does not change but the wall energy density varies in space (Figure 11c). The variation of the chemical heterogeneity can give rise to pinning and depinning effect as well, as can be seen in Equation (9). This explains that both mechanical and chemical patterns can lead to the pinning and depinning effect. For mechanically patterned substrate, the change of the normal vectors due to the topological defects is consistent with the theories of Huh and Mason that the apparent contact angle is caused by the topological peaks and pitches. The term of normal vector has to work with the wall energy together to achieve an apparent contact angle. The variation in the wall energy due to chemical defects is consistent with the theories of de-Gennes-Brochard-Wyart-Quééré-Joanny and Marmur.

Apart from substrate  $S$ , the energy minimization has to be considered in the domain  $\Omega$  as well, which is especially important when phase transformation takes place. This energy minimization determines the shape for the cap of the liquid–gas. The evolution equation in the domain  $\Omega$  via diffusion in principle is governed by the diffusion equation of Fick's law. In the wetting phenomenon, two immiscible phases, for example, water/air, are present where the effect of the surface/interfacial tension comes into play. The surface tension effect has not been considered in the diffusion equation of Fick's law; a boundary condition, like Young–Laplace equation, or Gibbs–Thomson condition has to be added to the Fick's diffusion equation. An alternative way is a generalized diffusion equation for the free energy minimization in the  $\Omega$  to obtain the equilibrium shape of the liquid structure. From the first part of Equation (8), one can choose the evolution equation as

$$\frac{d\rho}{dt} = \nabla \cdot M \nabla \left( \frac{\partial f}{\partial \rho} - \nabla \cdot \frac{\partial f}{\partial \nabla \rho} \right) \quad (10)$$

By using the Leibniz integration and using the no-flux boundary condition, the free energy minimization in domain  $\Omega$  is achieved,  $-\int_{\Omega} M (\nabla \mu)^2 \leq 0$  for a positive mobility  $M$ . Here, the chemical

potential  $\mu$  is defined by the expression inside the bracket of the first term in Equation (8). This definition is nothing but the variational derivative or functional derivative. If the Cahn free energy density  $f(\rho, \frac{1}{2}\xi(\nabla\rho)^2)$  is used ( $\xi$  is a parameter related to the surface tension), we obtain the well-known Cahn–Hilliard model which has been widely used for the modeling of wetting phenomenon.<sup>[181–187]</sup> The advantage of Equation (10) over the conventional Fick’s diffusion equation is the consideration of the surface/interfacial tension effect, which is essential for the wetting phenomenon. Equations (9) and (10) consist of the thermodynamic description for the wetting effect. The thermodynamic description should be general for modeling the wetting phenomenon to address the equilibrium morphology of liquid structures. However, the kinetic energy due to convection has been overlooked in the thermodynamic description. The convection can be either external or intrinsic. In the latter case, the kinetic energy is exchanged with the interfacial free energy, which can change the metastable state. For instance, if a deformed water droplet is released on a homogeneous substrate, the droplet evolves towards the equilibrium with a certain velocity due to the Kortweg stress. When the velocity is relatively small, the droplet reaches the energy minima state of a spherical cap. When the velocity is relatively high corresponding to a large Weber number, the droplet can break up into separate small droplets, transforming the system from a low free energy state (a single droplet) to a high free energy state (two separate droplets). In this case, one has to consider not only the energy barrier but also the kinetics.

## 7. Conclusion and Outlook

We have overviewed recent progresses of wetting effect on patterned substrates starting from the classic Cassie–Wenzel theory. Based on the Cassie equation, one can design superhydrophobic substrate from a hydrophilic material by controlling the solid–liquid contact area and the intrinsic Young’s contact angle. Reducing the solid–liquid contact area can increase the hydrophobicity, but often leads to fragile structures which are mechanically unstable. A comprise of wettability and mechanical durability has been considered in ref. [113], engendering robust superhydrophobic metals, ceramic, and glass. Another application of the Cassie–Wenzel theory for materials design is coating via manipulating the contact area and the surface chemistry.<sup>[160]</sup> By stretching and releasing the coated polyester fabrics, the contact area between the liquid and the coated/uncoated fabrics is varied. The variation of the contact area leads to the reversible transition between Wenzel and Cassie states. The robustness factor has been introduced to measure the effectiveness of hydrophobicity when the materials are elongated in the stretched state.

Cassie equation has been often used to explain the superhydrophobic property of some plants in nature,<sup>[188]</sup> such as lotus leaves<sup>[189,190]</sup> and rose petals.<sup>[55]</sup> It has been illustrated that the lotus effect is caused by the two-level roughness. The micrometer scale bumps and the nanometer scale hair-like structures allow air to be trapped beneath the water droplets sitting on the leaf, forming the so-called Cassie state. The two-level roughness reduces the real contact area between the droplet and the leaf, which leads to a superhydrophobic structure. It comes to a question whether the lotus leaf is always superhydrophobic. According to Cassie’s equation, when the contact area is large,

we achieve the intrinsic wettability. It has been experimentally shown in ref. [191] that lotus leaf can be hydrophilic if water drops are trapped in between the surface micro/nano-pillars during condensation. This is because the surface of the nano-hairy structures or porous structures is not intrinsically hydrophobic, as measured in ref. [191].

The limitation of Cassie–Wenzel theory has been overviewed and some open questions are left. Based on the axiom of energy minimization principle, the wetting state is addressed by the energy minimum states. There are three contributions to the system energy, liquid–gas cap, liquid–solid contact area, and gas–solid contact area. Note that the gas–solid contact area is not only outside the triple line but also beneath the droplet in the pore for mechanically structured surface. The main challenge here is to measure the liquid–solid and the gas–liquid contact areas beneath the droplet. The liquid can partially penetrate into the pore, resulting in a meniscus with non-zero mean curvature. The resulting Young–Laplace pressure due to this curvature should be identical to the pressure ascribe to the curved liquid–gas cap to establish a stable droplet state. The model proposed by Nagayama and Zhang<sup>[112]</sup> has been used to calculate the apparent contact angle by using the effective wetting ratio  $f$ , demonstrating the existence of intermediate wetting states. This model has been shown to be good consistent with experiments. However, the effective wetting ratio  $f$  is really hard to be measured for a real complex substrate. By this way, it is hard to address how many intermediate states exist beyond the Cassie and Wenzel theory and which state is the most stable one. Another difficulty to address the intermediate states is the liquid–gas cap, which is not necessary to be spherical. Especially near the base area, the liquid–gas interface can be deformed, becoming anisotropic.

One open question has not yet been addressed by the Cassie–Wenzel theory is the state of the gas beneath the droplet. It is often interpreted that at the Wenzel state, the liquid completely contacts the solid substrate and the real contact area is corrected by the roughness factor. However, it is unclear how the gas evolves when the Wenzel state originates from the Cassie state. In the Cassie state, the gas fills in the pore beneath the droplet, providing support for the stability of the droplet. Some literature has been devoted to address this question.<sup>[153,192,193]</sup> The gas state can be classified into three categories: i) The gas in the pore is compressed.<sup>[153,192]</sup> In this case, one has to consider the state equation of the gas. The resulting pressure provides support of the droplet, leading to intermediate wetting states. For this state, one has to study the penetration of the droplet at the pore level. A recent paper addressed the capillary adsorption criterion of a droplet penetrating into the pore structure, where the influence of droplet size, Young’s contact angle, and the opening angle of the pore is revealed.<sup>[194]</sup> ii) When the droplet gradually spreads outward, the gas in the pore beneath the droplet moves toward the triple line region and is extruded to the surroundings. iii) The gas dissolves into the liquid, forming gas bubbles.<sup>[153,193]</sup>

The applicability of the Cassie–Wenzel theory is for droplet size much larger than the characteristic length of the surface heterogeneity. When the droplet size is comparable to the one of the heterogeneity, anisotropic wetting morphologies are usually observed. In this case, the wetting pattern is affected by the droplet volume, the deposition position, the arrangement/orientation of the heterogeneity, and the size/mean curvature of the

heterogeneity. In this report, we have reviewed the anisotropic wetting morphologies on: i) stripped/lattice/chessboard chemically patterned substrate; ii) mechanically patterned substrates with square/triangular/hexagonal arrangement of the heterogeneity; and iii) 3D capillary ratchet. In case (i), a combination of analytical model, numerical simulation, and experiment shows the capability to identify rationally systematical wetting morphologies. By using the energy map method to guide the aspect ratio of the base area at the metastable states, simulations and experiments are performed by controlling the initial shape of the liquid structure; numerous anisotropic wetting morphologies are achieved. However, it remains an open question to address the axially symmetrical anisotropic wetting morphologies. The difficulty is the same as the Cassie–Wenzel theory, where the real contact area and the curve of contact line are challenging to be prescribed analytically. Numerical simulation may be an approach to solve this problem. In case (ii), the anisotropic wetting shape is mainly controlled by the arrangement of the micropillars rather than the shape of the heterogeneity. For instance, two hydrophilic spots lead to a line wetting shape; a triangular arrangement of the pillars results in triangle wetting morphologies, etc. The key point here is to control the system to achieve either the Cassie or the Wenzel state. At the Wenzel state, the droplet takes the shape according to the arrangement of the heterogeneity. In case (iii), an araucaria leaf inspired surface has been designed, which shows well-controlled directional movement of liquids. The controlling parameter is the tiling angle of the araucaria leaf and the Young's contact angle.

All these wetting effects on patterned substrate come to the key question of the metastable states and the energy barriers, which are caused by the surface heterogeneity. By varying the surface from ideally smooth to heterogeneous, the energy minimum state changes from unique in Young's law to numerous, such as Cassie state, Wenzel state, and many other intermediate states. The numerous metastable states make the diversity of the wetting morphologies and provide immense opportunities for materials design in different fields with distinct functionalities; but the control of the metastable states and the design are a long way to go. The present overview focuses on the quasi-equilibrium wetting effect, where the inertial effect, viscous effect, and gravity effect are mostly overlooked. The wetting morphology can spontaneously transform between different metastable states, making the situation even more complex. An interdisciplinary study of the wetting effect with scientists from different fields is required to surmount these challenges.

## Acknowledgements

F.W. is grateful to the VirtMat project "VirtMat P09: Wetting Phenomena" of the Helmholtz association. Y.W. thanks the funding of the research through the Gottfried-Wilhelm Leibniz prize NE 822/31-1 of the German Research Foundation (DFG). The authors thank F. Guo for partially editing the figures. The authors acknowledge support by the state of Baden-Wuerttemberg through bwHPC.

Open access funding enabled and organized by Projekt DEAL.

## Conflict of Interest

The authors declare no conflict of interest.

## Keywords

anisotropic wetting morphology, patterned substrates, wetting

Received: November 18, 2022

Revised: January 1, 2023

Published online:

- [1] P.-G. De Gennes, F. Brochard-Wyart, D. Quéré, *Capillarity and Wetting Phenomena: Drops, Bubbles, Pearls, Waves*, vol. 315, Springer, Berlin, Germany **2004**.
- [2] J. Li, X. Han, W. Li, L. Yang, X. Li, L. Wang, *Prog. Mater. Sci.* **2022**, *133*, 101064.
- [3] B. Andreotti, J. H. Snoeijer, *Annu. Rev. Fluid Mech.* **2020**, *52*, 285.
- [4] E. Arzt, H. Qian, R. M. McMeeking, R. Hensel, *Prog. Mater. Sci.* **2021**, *120*, 100823.
- [5] M. Li, C. Li, B. R. Blackman, S. Eduardo, *Int. Mater. Rev.* **2021**, *67*, 658.
- [6] T. Darmanin, F. Guittard, *Mater. Today* **2015**, *18*, 273.
- [7] A. Samanta, Q. Wang, S. K. Shaw, H. Ding, *Mater. Des.* **2020**, *192*, 108744.
- [8] X.-Q. Zhao, F. Wahid, J.-X. Cui, Y.-Y. Wang, C. Zhong, *Int. J. Biol. Macromol.* **2021**, *185*, 890.
- [9] H.-P. Lin, L.-J. Chen, *J. Colloid Interface Sci.* **2021**, *603*, 539.
- [10] M. Kim, S. Yoo, H. E. Jeong, M. K. Kwak, *Nat. Commun.* **2022**, *13*, 5181.
- [11] Y. Xiang, S. Huang, T.-Y. Huang, A. Dong, D. Cao, H. Li, Y. Xue, P. Lv, H. Duan, *Proc. Natl. Acad. Sci. USA* **2020**, *117*, 2282.
- [12] Z. Li, K. Zhao, Y. Wang, Z. Zheng, C. Zhang, Y. Gao, F. Du, *Colloids Surf., A* **2022**, 129178.
- [13] R. Jiang, L. Hao, L. Song, L. Tian, Y. Fan, J. Zhao, C. Liu, M. W., L. Ren, *Chem. Eng. J.* **2020**, *398*, 125609.
- [14] L. Yang, X. Shen, Q. Yang, J. Liu, W. Wu, D. Li, J. Du, B. Zhang, S. Fan, *Opt. Mater.* **2021**, *112*, 110740.
- [15] L. Zheng, C. Cao, Z. Chen, L. Cao, Q. Huang, B. Song, *Pest Manage. Sci.* **2021**, *77*, 3198.
- [16] D. Gao, J. Chen, W. Qian, Y. He, P. Song, R. Wang, *Waste Biomass Valorization* **2020**, *11*, 6993.
- [17] E. Alizadeh-Birjandi, F. Tavakoli-Dastjerdi, J. S. Leger, K. F. Faull, S. H. Davis, J. P. Rothstein, H. Pirouz Kavehpour, *Eur. Phys. J.: Spec. Top.* **2020**, *229*, 1881.
- [18] C. Shao, Y. Liu, J. Chi, Z. Chen, J. Wang, Y. Zhao, *Langmuir* **2019**, *35*, 3832.
- [19] S. Dong, X. Zhang, Q. Li, C. Liu, T. Ye, J. Liu, H. Xu, X. Zhang, J. Liu, C. Jiang, L. Xue, S. Yang, X. Xiao, *Small* **2020**, *16*, 2000779.
- [20] S. Singla, D. Jain, C. M. Zoltowski, S. Voleti, A. Y. Stark, P. H. Niewiarowski, A. Dhinojwala, *Sci. Adv.* **2021**, *7*, eabd9410.
- [21] H.-W. Chien, X.-Y. Chen, W.-P. Tsai, M. Lee, *Colloids Surf., B* **2020**, *186*, 110738.
- [22] D. G. Stavenga, J. Tinbergen, H. L. Leertouwer, B. D. Wilts, *J. Exp. Biol.* **2011**, *214*, 3960.
- [23] X. Zeng, L. Qian, X. Yuan, C. Zhou, Z. Li, J. Cheng, S. Xu, S. Wang, P. Pi, X. Wen, *ACS Nano* **2017**, *11*, 760.
- [24] J. Guadarrama-Cetina, A. Mongruel, M.-G. Medici, E. Baquero, A. Parker, I. Milimouk-Melnytschuk, W. González-Viñas, D. Beysens, *Eur. Phys. J. E* **2014**, *37*, 109.
- [25] Z. Chen, Z. Zhang, *Water Sci. Technol.* **2020**, *82*, 207.
- [26] J. Lei, Z. Guo, *Nanoscale* **2020**, *12*, 6921.
- [27] M. Wang, Z. Zhang, Y. Wang, X. Zhao, M. Yang, X. Men, Q. Xue, *Chem. Eng. J.* **2020**, *384*, 123292.
- [28] J. Drelich, A. Marmur, *Surf. Innovations* **2014**, *2*, 211.

- [29] X. Hu, Y. Yu, Y. Wang, Y. Wang, J. Zhou, L. Song, *Mater. Lett.* **2016**, *182*, 372.
- [30] C. Walker, E. Mitridis, T. Kreiner, H. Eghlidi, T. M. Schutzius, D. Poulidakos, *Nano Lett.* **2019**, *19*, 1595.
- [31] A. Mishra, V. Rathi, *Int. J. Eng. Res. Electr. Electron. Eng.* **2017**, *4*, 2395.
- [32] F. Geyer, M. D'Acunzi, A. Sharifi-Aghili, A. Saal, N. Gao, A. Kaltbeitzel, T.-F. Sloot, R. Berger, H.-J. Butt, D. Vollmer, *Sci. Adv.* **2020**, *6*, eaaw9727.
- [33] C. Yu, S. Sasic, K. Liu, S. Salameh, R. H. Ras, J. R. van Ommen, *Chem. Eng. Res. Des.* **2020**, *155*, 48.
- [34] A. S. Sarkin, N. Ekren, Ş. Sağlam, *Sol. Energy* **2020**, *199*, 63.
- [35] A. Behera, in *Advanced Materials*, Springer, Berlin, Germany **2022**, pp. 359–394.
- [36] S. Huang, R. H. Ras, X. Tian, *Curr. Opin. Colloid Interface Sci.* **2018**, *36*, 90.
- [37] W. Deng, G. Wang, L. Tang, Z. Zeng, T. Ren, *J. Colloid Interface Sci.* **2022**, *608*, 186.
- [38] L. Zheng, K. Wang, D. Hou, X. Jia, Z. Zhao, *Desalination* **2022**, *526*, 115512.
- [39] Z. Han, X. Feng, Z. Guo, S. Niu, L. Ren, *Adv. Mater.* **2018**, *30*, 1704652.
- [40] J. Yoon, M. Ryu, H. Kim, G.-N. Ahn, S.-J. Yim, D.-P. Kim, H. Lee, *Adv. Mater.* **2020**, *32*, 2002710.
- [41] R. Ogaki, M. Alexander, P. Kingshott, *Mater. Today* **2010**, *13*, 22.
- [42] M. Soltani, K. Golovin, *Adv. Funct. Mater.* **2022**, *32*, 2107465.
- [43] D. Chen, G. H. McKinley, R. E. Cohen, *Proc. Natl. Acad. Sci. USA* **2016**, *113*, 8087.
- [44] X. Jing, W. Si, J. Sun, J. Zhou, J. Lin, B. Yu, M. Lu, *Adv. Mater. Interfaces* **2022**, *9*, 2101231.
- [45] A. Shome, A. Das, A. Borbora, M. Dhar, U. Manna, *Chem. Soc. Rev.* **2022**, *51*, 5452.
- [46] E. Chen, Q. Yuan, Y.-P. Zhao, *Soft Matter* **2018**, *14*, 6198.
- [47] Z. Liu, T. Niu, Y. Lei, Y. Luo, *Biosurf. Biotribol.* **2022**.
- [48] C. Duez, C. Ybert, C. Clanet, L. Bocquet, *Phys. Rev. Lett.* **2010**, *104*, 084503.
- [49] A. Nilghaz, L. Zhang, W. Shen, *Chem. Eng. Sci.* **2015**, *129*, 34.
- [50] Y. Kawahara, S. Hodges, B. S. Cook, C. Zhang, G. D. Abowd, in *Ubi-Comp '13: Proc. 2013 ACM Int. Joint Conf. on Pervasive and Ubiquitous Computing*, ACM, New York **2013**, pp. 363–372.
- [51] T. Young, *Philos. Trans. R. Soc. London* **1805**, *95*, 65.
- [52] R. N. Wenzel, *Ind. Eng. Chem.* **1936**, *28*, 988.
- [53] A. Cassie, S. Baxter, *Trans. Faraday Soc.* **1944**, *40*, 546.
- [54] K. Koch, B. Bhushan, W. Barthlott, *Prog. Mater. Sci.* **2009**, *54*, 137.
- [55] M. Chakraborty, J. A. Weibel, J. A. Schaber, S. V. Garimella, *Adv. Mater. Interfaces* **2019**, *6*, 1900652.
- [56] Y. Yang, Z. Guo, W. Liu, *Small* **2022**, 2204624.
- [57] H. Grewal, P. Pendyala, H. Shin, I.-J. Cho, E.-S. Yoon, *Wear* **2017**, *384*, 151.
- [58] J. Chen, Z. Wang, C. Liu, Z. Chen, X. Tang, Q. Wu, S. Zhang, G. Song, S. Cong, Q. Chen, Z. Zhao, *Adv. Mater.* **2021**, *33*, 2007314.
- [59] X. Liu, D. Wang, Z. Yang, H. Zhou, Q. Zhao, T. Fan, *Adv. Opt. Mater.* **2019**, *7*, 1900687.
- [60] M. I. Osotsi, W. Zhang, I. Zada, J. Gu, Q. Liu, D. Zhang, *Natl. Sci. Rev.* **2021**, *8*, nwa107.
- [61] Z. Chen, F. Fu, Y. Yu, H. Wang, Y. Shang, Y. Zhao, *Adv. Mater.* **2019**, *31*, 1805431.
- [62] Z. Chen, Z. Zhang, Y. Wang, D. Xu, Y. Zhao, *Mater. Sci. Eng., R* **2021**, *144*, 100605.
- [63] D. Zhang, S. Takase, G. Nagayama, *J. Colloid Interface Sci.* **2021**, *591*, 474.
- [64] Y. Cai, L. Lin, Z. Xue, M. Liu, S. Wang, L. Jiang, *Adv. Funct. Mater.* **2014**, *24*, 809.
- [65] M. Yu, Q. Wang, W. Yang, Y. Xu, M. Zhang, Q. Deng, G. Liu, *Polymers* **2019**, *11*, 442.
- [66] S. Liu, X. Liu, S. S. Latthe, L. Gao, S. An, S. S. Yoon, B. Liu, R. Xing, *Appl. Surf. Sci.* **2015**, *351*, 897.
- [67] L. Xi, I. Kaban, R. Nowak, G. Bruzda, N. Sobczak, J. Eckert, *J. Am. Ceram. Soc.* **2018**, *101*, 911.
- [68] F. Wang, A. Reiter, M. Kellner, J. Brillo, M. Selzer, B. Nestler, *Acta Mater.* **2018**, *146*, 106.
- [69] E. Bormashenko, *J. Colloid Interface Sci.* **2019**, *537*, 597.
- [70] B. Laing, D. Seveno, J. De Keyser, A. Van Bael, *Colloid Interface Sci. Commun.* **2021**, *40*, 100343.
- [71] M. Hartmann, S. Hardt, *Langmuir* **2019**, *35*, 4868.
- [72] A. Maliješský, A. O. Parry, M. Pospíšil, *Phys. Rev. E* **2019**, *99*, 042804.
- [73] A. Russo, M. Icardi, M. Elsharkawy, D. Ceglia, P. Asinari, C. M. Megaridis, *Phys. Rev. Fluids* **2020**, *5*, 074002.
- [74] M. Ewetola, R. Ledesma-Aguilar, M. Pradas, *Phys. Rev. Fluids* **2021**, *6*, 033904.
- [75] D. Groves, N. Savva, *Phys. Rev. Fluids* **2021**, *6*, 123601.
- [76] S. Son, J. Carmeliet, L. Chen, Q. Kang, D. Derome, *Langmuir* **2021**, *37*, 2541.
- [77] Y. Yu, Q. Li, C. Q. Zhou, P. Zhou, H. Yan, *Appl. Therm. Eng.* **2017**, *127*, 1346.
- [78] B. He, C. Qin, S. Zhou, B. Wen, *Phys. Rev. Fluids* **2020**, *5*, 114003.
- [79] Y. Wu, F. Wang, M. Selzer, B. Nestler, *Langmuir* **2019**, *35*, 8500.
- [80] Y. Wu, F. Wang, M. Selzer, B. Nestler, *Phys. Rev. E* **2019**, *100*, 041102.
- [81] Y. Wu, F. Wang, S. Ma, M. Selzer, B. Nestler, *Soft Matter* **2020**, *16*, 6115.
- [82] Y. Wu, M. Kuzina, F. Wang, M. Reischl, M. Selzer, B. Nestler, P. A. Levkin, *J. Colloid Interface Sci.* **2022**, *606*, 1077.
- [83] I. Dević, G. Soligno, M. Dijkstra, R. v. Roij, X. Zhang, D. Lohse, *Langmuir* **2017**, *33*, 2744.
- [84] I. U. Chowdhury, P. S. Mahapatra, A. K. Sen, A. Pattamatta, M. K. Tiwari, *Phys. Rev. Fluids* **2021**, *6*, 094003.
- [85] X. Geng, Y. Xing, J. Huan, Y. Hou, Y. Zheng, *Adv. Mater. Interfaces* **2022**, *10*, 2201978.
- [86] H. P. Jansen, K. Sotthewes, C. Ganser, H. J. W. Zandvliet, C. Teichert, E. S. Kooij, *Langmuir* **2014**, *30*, 11574.
- [87] H. P. Jansen, H. J. Zandvliet, E. S. Kooij, *Int. J. Heat Mass Transfer* **2015**, *82*, 537.
- [88] H. Patrick Jansen, K. Sotthewes, H. J. Zandvliet, E. S. Kooij, *Appl. Surf. Sci.* **2016**, *361*, 122.
- [89] S. Varagnolo, V. Schiocchet, D. Ferraro, M. Pierno, G. Mistura, M. Sbragaglia, A. Gupta, G. Amati, *Langmuir* **2014**, *30*, 2401.
- [90] X. Chen, R. Ma, J. Li, C. Hao, W. Guo, B. L. Luk, S. C. Li, S. Yao, Z. Wang, *Phys. Rev. Lett.* **2012**, *109*, 116101.
- [91] M. Amabili, A. Giacomello, S. Meloni, C. M. Casciola, *Phys. Rev. Fluids* **2017**, *2*, 034202.
- [92] S.-H. Lv, F.-F. Xie, Y.-R. Yang, D.-J. Lee, X.-D. Wang, Y.-Y. Duan, *Phys. Rev. Fluids* **2022**, *7*, 034203.
- [93] S. Iliev, N. Pesheva, P. Iliev, *Phys. Rev. E* **2018**, *97*, 042801.
- [94] A. Gupta, H. Lee, P. S. Doyle, *Phys. Rev. Fluids* **2017**, *2*, 094007.
- [95] J. Li, X. Zhou, J. Li, L. Che, J. Yao, G. McHale, M. K. Chaudhury, Z. Wang, *Sci. Adv.* **2017**, *3*, eaao3530.
- [96] C. Li, C. Yu, S. Zhou, Z. Dong, L. Jiang, *Proc. Natl. Acad. Sci. USA* **2020**, *117*, 23436.
- [97] S. Feng, P. Zhu, H. Zheng, H. Zhan, C. Chen, J. Li, L. Wang, X. Yao, Y. Liu, Z. Wang, *Science* **2021**, *373*, 1344.
- [98] C. Lin, K. Zhang, X. Chen, L. Xiao, S. Chen, J. Zhu, T. Zou, *Phys. Rev. Fluids* **2021**, *6*, 083602.
- [99] T. L. Liu, C.-J. C. Kim, *Science* **2014**, *346*, 1096.
- [100] L. Wang, R. Wang, J. Wang, T.-S. Wong, *Sci. Adv.* **2020**, *6*, eabb2307.
- [101] L. Sun, F. Bian, Y. Wang, Y. Wang, X. Zhang, Y. Zhao, *Proc. Natl. Acad. Sci. USA* **2020**, *117*, 4527.
- [102] P. Lv, Y. Xue, Y. Shi, H. Lin, H. Duan, *Phys. Rev. Lett.* **2014**, *112*, 196101.

- [103] W. Xu, Y. Liu, B. Xiao, H. Jiang, M. Chen, Y. Wang, *Adv. Mater. Interfaces* **2021**, *8*, 2100174.
- [104] S. Kim, Z. Wu, E. Esmaili, J. J. Dombroskie, S. Jung, *Proc. Natl. Acad. Sci. USA* **2020**, *117*, 13901.
- [105] R. Raj, S. Adera, R. Enright, E. N. Wang, *Nat. Commun.* **2014**, *5*, 4975.
- [106] J. Lou, S. Shi, C. Ma, X. Zhou, D. Huang, Q. Zheng, C. Lv, *Nat. Commun.* **2022**, *13*, 2685.
- [107] A. U. Siddique, M. Trimble, F. Zhao, M. M. Weislogel, H. Tan, *Phys. Rev. Fluids* **2020**, *5*, 063606.
- [108] M. Liu, J. Li, X. Zhou, J. Li, S. Feng, Y. Cheng, S. Wang, Z. Wang, *Adv. Mater.* **2020**, *32*, 1907999.
- [109] D. Murakami, H. Jinnai, A. Takahara, *Langmuir* **2014**, *30*, 2061.
- [110] X. Dai, N. Sun, S. O. Nielsen, B. B. Stogin, J. Wang, S. Yang, T.-S. Wong, *Sci. Adv.* **2018**, *4*, eaq0919.
- [111] G.-T. Yun, W.-B. Jung, M. S. Oh, G. M. Jang, J. Baek, N. I. Kim, S. G. Im, H.-T. Jung, *Sci. Adv.* **2018**, *4*, ea4978.
- [112] G. Nagayama, D. Zhang, *Soft Matter* **2020**, *16*, 3514.
- [113] D. Wang, Q. Sun, M. J. Hokkanen, C. Zhang, F.-Y. Lin, Q. Liu, S.-P. Zhu, T. Zhou, Q. Chang, B. He, Q. Zhou, L. Chen, Z. Wang, R. H. A. Ras, X. Deng, *Nature* **2020**, *582*, 55.
- [114] A. Marmur, C. Della Volpe, S. Siboni, A. Amirfazli, J. W. Drelich, *Surf. Innovations* **2017**, *5*, 3.
- [115] R. Tadmor, *Langmuir* **2004**, *20*, 7659.
- [116] S. Parvate, P. Dixit, S. Chattopadhyay, *J. Phys. Chem. B* **2020**, *124*, 1323.
- [117] J. W. Drelich, *Adv. Colloid Interface Sci.* **2019**, *267*, 1.
- [118] G. Whyman, E. Bormashenko, T. Stein, *Chem. Phys. Lett.* **2008**, *450*, 355.
- [119] Y. Peng, W. Zhu, S. Shen, L. Feng, Y. Deng, *Adv. Mater. Interfaces* **2017**, *4*, 1700497.
- [120] G. Wang, Z. Guo, W. Liu, *J. Bionic Eng.* **2014**, *11*, 325.
- [121] M. Zhang, S. Feng, L. Wang, Y. Zheng, *Biotribology* **2016**, *5*, 31.
- [122] Z. Han, J. Fu, Z. Wang, Y. Wang, B. Li, Z. Mu, J. Zhang, S. Niu, *Colloids Surf., A* **2017**, *518*, 139.
- [123] G. S. Watson, D. W. Green, B. W. Cribb, C. L. Brown, C. R. Meritt, M. J. Tobin, J. Vongsivut, M. Sun, A.-P. Liang, J. A. Watson, *ACS Appl. Mater. Interfaces* **2017**, *9*, 24381.
- [124] E. Bormashenko, *J. Adhes. Sci. Technol.* **2020**, *34*, 219.
- [125] C. Sun, J. McClure, S. Berg, P. Mostaghimi, R. T. Armstrong, *J. Colloid Interface Sci.* **2022**, *608*, 2330.
- [126] L. Gao, T. J. McCarthy, *Langmuir* **2006**, *22*, 2966.
- [127] Y. Jiang, C.-H. Choi, *Adv. Mater. Interfaces* **2021**, *8*, 2001205.
- [128] R. Tadmor, *Langmuir* **2021**, *37*, 6357.
- [129] C. Huh, S. Mason, *J. Colloid Interface Sci.* **1977**, *60*, 11.
- [130] A. Marmur, *Colloids Surf., A* **1998**, *136*, 209.
- [131] C. Furmidge, *J. Colloid Sci.* **1962**, *17*, 309.
- [132] K. Kawasaki, *J. Colloid Sci.* **1960**, *15*, 402.
- [133] C. Extrand, A. Gent, *J. Colloid Interface Sci.* **1990**, *138*, 431.
- [134] R. Tadmor, P. Bahadur, A. Leh, H. E. N'guessan, R. Jaini, L. Dang, *Phys. Rev. Lett.* **2009**, *103*, 266101.
- [135] E. Bormashenko, G. Chaniel, R. Gryniov, *Appl. Surf. Sci.* **2013**, *273*, 549.
- [136] W. Xu, J. Xu, X. Li, Y. Tian, C.-H. Choi, E.-H. Yang, *Soft Matter* **2016**, *12*, 6902.
- [137] M. Reyssat, D. Quéré, *J. Phys. Chem. B* **2009**, *113*, 3906.
- [138] E. Bormashenko, R. Pogreb, G. Whyman, M. Erlich, *Langmuir* **2007**, *23*, 6501.
- [139] J. Ren, F. Duan, *Curr. Opin. Colloid Interface Sci.* **2021**, *53*, 101425.
- [140] M. Ewetola, R. Ledesma-Aguilar, M. Pradas, *Phys. Rev. Fluids* **2021**, *6*, 033904.
- [141] X. Yan, Z. Huang, S. Sett, J. Oh, H. Cha, L. Li, L. Feng, Y. Wu, C. Zhao, D. Orejon, F. Chen, N. Miljkovic, *ACS Nano* **2019**, *13*, 4160.
- [142] Q. Peng, L. Jia, Y. Ding, C. Dang, L. Yin, X. Yan, *Int. Commun. Heat Mass Transfer* **2020**, *112*, 104492.
- [143] D. Khilif, W. Foudhil, S. Harmand, S. B. Jabrallah, *Int. J. Therm. Sci.* **2020**, *151*, 106236.
- [144] R. Tekidou, G. Duursma, C. Mackenzie-Dover, V. Kubyskhina, J. Terry, K. Sefiane, *Heat Transfer Eng.* **2020**, *41*, 1645.
- [145] L. Sun, J. Guo, H. Chen, D. Zhang, L. Shang, B. Zhang, Y. Zhao, *Adv. Sci.* **2021**, *8*, 2100126.
- [146] H. Li, A. Li, Z. Zhao, L. Xue, M. Li, Y. Song, *Acc. Mater. Res.* **2021**, *2*, 230.
- [147] A. Russo, M. Icardi, M. Elsharkawy, D. Ceglia, P. Asinari, C. M. Megaridis, *Phys. Rev. Fluids* **2020**, *5*, 074002.
- [148] C. Lin, K. Zhang, X. Chen, L. Xiao, S. Chen, J. Zhu, T. Zou, *Phys. Rev. Fluids* **2021**, *6*, 083602.
- [149] L. Wang, R. Wang, J. Wang, T.-S. Wong, *Sci. Adv.* **2020**, *6*, eabb2307.
- [150] O. Ramirez-Soto, V. Sanjay, D. Lohse, J. T. Pham, D. Vollmer, *Sci. Adv.* **2020**, *6*, eaba4330.
- [151] S. Kim, Z. Wu, E. Esmaili, J. J. Dombroskie, S. Jung, *Proc. Natl. Acad. Sci. USA* **2020**, *117*, 13901.
- [152] M. Liu, J. Li, X. Zhou, J. Li, S. Feng, Y. Cheng, S. Wang, Z. Wang, *Adv. Mater.* **2020**, *32*, 1907999.
- [153] C. Ran, G. Ding, W. Liu, Y. Deng, W. Hou, *Langmuir* **2008**, *24*, 9952.
- [154] B. Hou, C. Wu, X. Li, J. Huang, M. Chen, *Appl. Surf. Sci.* **2021**, *542*, 148611.
- [155] M. Dicuango, S. Dash, J. A. Weibel, S. V. Garimella, *Appl. Phys. Lett.* **2014**, *104*, 201604.
- [156] A. Lafuma, D. Quéré, *Nat. Mater.* **2003**, *2*, 457.
- [157] K. Lewis, T. Matsuura, *ACS Omega* **2022**, *7*, 36510.
- [158] K. Doudrick, S. Liu, E. M. Mutunga, K. L. Klein, V. Damle, K. K. Varanasi, K. Rykaczewski, *Langmuir* **2014**, *30*, 6867.
- [159] V. Sharma, D. S. Patel, M. Gyanprakash, J. Ramkumar, *Surf. Coat. Technol.* **2021**, *422*, 127533.
- [160] S. Pan, R. Guo, M. Björnalm, J. J. Richardson, L. Li, C. Peng, N. Bertleff-Zieschang, W. Xu, J. Jiang, F. Caruso, *Nat. Mater.* **2018**, *17*, 1040.
- [161] H. P. Jansen, K. Sotthewes, J. van Swigchem, H. J. Zandvliet, E. S. Kooij, *Phys. Rev. E* **2013**, *88*, 013008.
- [162] Q. Li, P. Zhou, H. Yan, *Langmuir* **2016**, *32*, 9389.
- [163] V. S. Ajaev, E. Y. Gatapova, O. A. Kabov, *Adv. Colloid Interface Sci.* **2016**, *228*, 92.
- [164] A. Dziedzic, M. Nakrani, B. Ezra, M. Syed, S. Popinet, S. Afkhami, *Eur. Phys. J. E* **2019**, *42*, 18.
- [165] J. Wang, Y. Wu, Y. Cao, G. Li, Y. Liao, *Colloid Polym. Sci.* **2020**, *298*, 1107.
- [166] L. Makkonen, *J. Chem. Phys.* **2017**, *147*, 064703.
- [167] D. Jacqmin, *J. Comput. Phys.* **1999**, *155*, 96.
- [168] D. M. Anderson, G. B. McFadden, A. A. Wheeler, *Annu. Rev. Fluid Mech.* **1998**, *30*, 139.
- [169] L. Wu, Z. Dong, M. Kuang, Y. Li, F. Li, L. Jiang, Y. Song, *Adv. Funct. Mater.* **2015**, *25*, 2237.
- [170] M. van Gorcum, B. Andreotti, J. H. Snoeijer, S. Karpitschka, *Phys. Rev. Lett.* **2018**, *121*, 208003.
- [171] J. W. Cahn, J. E. Hilliard, *J. Chem. Phys.* **1958**, *28*, 258.
- [172] N. Provatas, K. Elder, *Phase-Field Methods in Materials Science and Engineering*, John Wiley & Sons, Hoboken, NJ, USA **2011**.
- [173] J. W. Cahn, *J. Chem. Phys.* **1977**, *66*, 3667.
- [174] P.-G. De Gennes, *Rev. Mod. Phys.* **1985**, *57*, 827.
- [175] F. Alpak, I. Zacharoudiou, S. Berg, J. Dietderich, N. Saxena, *Comput. Geosci.* **2019**, *23*, 849.
- [176] G. Zhu, J. Kou, J. Yao, A. Li, S. Sun, *J. Comput. Phys.* **2020**, *405*, 109170.
- [177] P. Yue, *J. Fluid Mech.* **2020**, *899*, A19.
- [178] K. Bazesefidpar, L. Brandt, O. Tammisola, *Int. J. Numer. Methods Fluids* **2022**, *94*, 1517.
- [179] H. G. Lee, J. Yang, S. Kim, J. Kim, *Appl. Math. Comput.* **2021**, *390*, 125591.

- [180] X. Xu, X. Wang, *SIAM J. Appl. Math.* **2011**, *71*, 1753.  
[181] R. Shimizu, H. Tanaka, *Sci. Adv.* **2017**, *3*, eaap9570.  
[182] P. Yue, J. J. Feng, *J. Non-Newtonian Fluid Mech.* **2012**, *189*, 8.  
[183] F. Wang, B. Nestler, *J. Chem. Phys.* **2021**, *154*, 094704.  
[184] J. Shen, X. Yang, H. Yu, *J. Comput. Phys.* **2015**, *284*, 617.  
[185] F. Wang, H. Zhang, Y. Wu, B. Nestler, *SSRN* **2022**, <http://doi.org/10.2139/ssrn.4206790>.  
[186] N. Bala, M. Pepona, I. Karlin, H. Kusumaatmaja, C. Semprebon, *Phys. Rev. E* **2019**, *100*, 013308.  
[187] S. F. Kalourazi, F. Wang, H. Zhang, M. Selzer, B. Nestler, *J. Phys.: Condens. Matter* **2022**, *34*, 444003.  
[188] C. Zhang, D. A. Mcadams, J. C. Grunlan, *Adv. Mater.* **2016**, *28*, 6292.  
[189] S. Sun, H. Li, Y. Guo, H.-Y. Mi, P. He, G. Zheng, C. Liu, C. Shen, *Prog. Org. Coat.* **2021**, *151*, 106090.  
[190] F. Zhao, F. Zhan, L. Wang, *Adv. Mater. Interfaces* **2022**, *10*, 2202044.  
[191] Y.-T. Cheng, D. E. Rodak, *Appl. Phys. Lett.* **2005**, *86*, 144101.  
[192] C. Luo, M. Xiang, X. Heng, *Langmuir* **2012**, *28*, 9554.  
[193] B. S. Sommers, J. E. Foster, N. Y. Babaeva, M. J. Kushner, *J. Phys. D: Appl. Phys.* **2011**, *44*, 082001.  
[194] Y. Wu, F. Wang, W. Huang, M. Selzer, B. Nestler, *Phys. Rev. Fluids* **2022**, *7*, 054004.



**Fei Wang** is a research scientist at the Karlsruhe Institute of Technology (KIT). His research interests span a wide range of fields including wetting, phase separation in polymers and metals, solidification, fluid dynamics, phase-field modeling. He completed his Ph.D. in the Department of Mechanical Engineering at KIT in 2017.



**Yanchen Wu** is a postdoctoral researcher in the Department of Mechanical Engineering at Karlsruhe Institute of Technology (KIT). He received his Ph.D. degree in mechanical engineering at KIT in 2021. His research interests include wetting, evaporation and condensation, multi-phase flow, fluid dynamics, and phase-field simulation.



**Britta Nestler** is a full professor for microstructure simulation in materials science at Karlsruhe Institute of Technology (KIT), the director of the Institute of Applied Materials-Microstructure Modelling and Simulation (IAM-MMS) at KIT, and the Institute of Digital Materials Science (IDM) at Karlsruhe University of Applied Sciences. She pursues research in multi-physics materials modeling and high-performance materials simulations.